

Late Reheating of the IGM by Quasars: A Radiation Hydrodynamical Simulation of Helium II Reionization

Pascal Paschos¹, Michael L. Norman^{1,2}, James O. Bordner¹ & Robert Harkness³

ABSTRACT

We study the ionization and thermal evolution of the intergalactic medium during the epoch of He II reionization by means of radiation hydrodynamical cosmological simulations. We post-process baryonic density fields from a standard optically-thin IGM simulation with a homogeneous galaxy-dominated UV background (UVB) which reionizes H I and He I at $z=6.5$ but does not have any contribution to the ionization of He II. Therefore, we suppress the He II photoheating contribution to the gas temperature due to the homogeneous UVB. Quasars are introduced as point sources throughout the 100 Mpc simulation volume located at cold dark matter (CDM) density peaks consistent with the Pei luminosity function. We assume an intrinsic quasar spectrum $J(\nu) \propto \nu^{-1.8}$ and a luminosity proportional to the halo mass. We evolve the spatial distribution of the He II ionizing radiation field at $h\nu = 4, 8$, and 16 Ryd using a time-implicit variable tensor Eddington factor radiative transfer scheme. Simultaneously, we also solve for the local ionization of He II to He III and the associated photoheating of the gas including opacity effects. We find that the percolation of the He III regions is essentially complete by $z=2.5$. When comparing to a self-consistent optically thin simulation at the same redshift, in which He II is also ionized by the uniform UVB, we find that inclusion of opacity effects results in higher IGM temperature by a factor of approximately 1.7 at the mean gas density level. We construct synthetic absorption line spectra from which we derive statistical parameters of the He II Ly α forest. We use 300 long ($\Delta z = 0.2$) random lines of sight to compute at $\bar{z} = 2.5 \pm 0.1$ a mean He II Ly α line transmission of $\bar{F} = 0.304 \pm 0.002$. The error corresponds to a significant one standard deviation in the transmitted flux due to the sightline to sightline variance equal to $\simeq 11\%$ the mean value. The opacity effect on the gas temperature is shown by comparing the broadening width of the H I and He II Ly α lines to the results from the self-consistent optically thin simulation. We find a shift by approximately 1.25 km/s to higher b-parameter values for both H I and He II. Finally, we estimate the relative broadening width between the

¹Laboratory for Computational Astrophysics,
Center for Astrophysics and Space Sciences,
University of California at San Diego, La Jolla, CA 92093, U.S.A.
Email: ppaschos, mlnorman, jbordner@ucsd.edu

²Physics Department, UCSD

³San Diego SuperComputer Center

two forests and find that the He II median b-parameter is about 0.8 times the median H I broadening width. This implies that the He II absorbers are physically extended consistent with conclusions from observed lines of sight.

Subject headings: cosmology: hydrodynamical simulations: radiation transfer

1. Introduction

The thermal evolution of the IGM after reionization is governed chiefly by photoheating (Efsthathiou 1992; Miralda-Escudé & Rees 1994). Models for the thermal evolution of the IGM (Miralda-Escudé & Ostriker 1990; Giroux & Shapiro 1996; Abel & Haehnelt 1999) generally assume that H I and He I are nearly fully ionized by $z \sim 6$ by star forming galaxies (Fan, Carilli & Keating 2006), while He II ionizes somewhat later at $z \sim 3$ by quasars due to He II's higher ionization potential and recombination rate (Sokasian, Abel & Hernquist 2002; hereafter SAH). Observational support for late He II reionization is summarized in SAH. Abel & Haehnelt (1999) emphasized the importance of opacity effects during reionization in establishing the post-reionization temperature of the gas. They showed that models using the optically thin expression for the photoheating rate during He II reionization underestimate the IGM temperature at mean density by a factor of ~ 2 .

Hydrodynamical cosmological simulations of the Ly α forest (Cen et al. 1994; Zhang, Anninos & Norman 1995; Hernquist et al. 1996; Miralda-Escudé et al. 1996; Zhang et al. 1997, 1998; Theuns et al. 1998) generally adopt the optically thin expression for photoheating for simplicity and computational economy. This is a reasonable assumption for the H I and He I photoheating at $z \sim 3$ due to the low opacity of the IGM, but not for the He II photoheating as He II is in the process of being ionized by the percolation of He III spheres (SAH). These simulations therefore underestimate the temperature of the IGM during the epoch of helium reionization. The standard approach taken in these simulations is to assume a homogeneous photoionizing background which evolves with redshift consistent with observed quasar and galaxy counts, such as that by Haardt & Madau (2001). The ionization and thermal state of the baryonic gas is then computed self-consistently with its dynamics by solving the equations of hydrodynamic cosmology including radiative heating and cooling (Cen 1992; Katz, Weinberg & Hernquist 1996; Anninos et al. 1997). It is found that the temperature of the low density IGM is determined almost entirely by photoheating balancing adiabatic cooling due to cosmic expansion. This results in a tight relationship between gas temperature and density, the so-called equation of state of the IGM (Hui & Gnedin 1997):

$$T = T_0 \Delta^\beta \quad (1)$$

where $\Delta = \rho/\bar{\rho}$ is the gas overdensity and β is redshift dependent but in the range $0 \leq \beta(z) \leq 0.6$. Abel & Haehnelt (1999) show that opacity effects during He II reionization raises T_0 and reduces β relative to an optically thin calculation. A technique often employed to include opacity effects within hydrodynamic simulations is to simply multiply the He II photoheating rate by a constant

factor $X_{\text{He II}} \geq 1$, with a value of 2-4 being sufficient to match observed temperatures (e.g., Bryan & Machacek 2000; Jena et al. 2005).

The combination of high spectral resolution quasar absorption line observations and hydrodynamical cosmological simulations provide a means for measuring the thermal evolution of the IGM. The thermal state of the gas is generally deduced from H I Ly α linewidths (b-values) in high resolution spectra (Rauch et al. 1997; Schaye et al. 1999, 2000; Bryan & Machacek 2000; Theuns et al. 2000; Bolton et al. 2005; Jena et al. 2005) although the flux power spectrum has also been employed (Zaldarriaga, Hui & Tegmark 2001). If the temperature of the IGM alone determined the b-values, then it would be straightforward to measure the temperature from high resolution spectra. However, Hubble broadening is always of the same order as the thermal broadening in Ly α forest absorption lines (Schaye 1999), hence the need for comparison with simulations. Theuns, Schaye & Haehnelt (2000) used the b-parameter distribution to measure the temperature of the IGM at $z=3.25$, finding $T_0 \geq 15,000$ K. Schaye et al. (2000) used the lower cutoff in the linewidth–column density scatter diagram to measure the temperature evolution of the IGM over the redshift range 2-4.5. They found evidence of late reheating at $z \sim 3$, which they ascribed to late He II reionization by quasars. Bryan & Machacek (2000) independently explored the same diagnostics and found that temperature estimates were sensitive to the assumed cosmology, in particular the amplitude of mass fluctuations on a few Mpc scales. Zaldarriaga, Hui & Tegmark (2001) used the falloff of the Ly α forest flux power spectrum at small scales to measure the IGM temperature, and found $T_0 \sim 2 \times 10^4$ K, dependent on their assumed β .

A proper calculation of He II reionization would treat quasars as point sources within the simulation volume and solve the equation of radiative transfer for the spatial distribution of the ionizing background coupled self-consistently to the dynamical, thermal, and ionization evolution of the gas. This was done in an approximate way by SAH, who post-processed a series of density fields taken from a SPH hydrodynamical simulation of the IGM using the GADGET code. The hydrodynamical simulation used the optically thin prescription for ionizing and heating the gas, assuming all ionization states of hydrogen and helium were in ionization equilibrium with the UVB of Haardt & Madau (1996). In the post-processing step, the helium reionization calculation was recomputed for an evolving quasar source population treated as point sources within the volume. Quasars were assumed to have a constant lifetime of 10^7 yr. Every 10^7 yr, peaks within the density field of a suitably chosen data dump from the hydrodynamic simulation were populated with quasars consistent with an empirical luminosity function. Around each point source the static equation of radiative transfer for He II ionizing photons was solved using a photon-conserving ray-casting scheme. The ionization state of He II was then updated ignoring thermal feedback to the gas. SAH found that for reasonable parameter choices, He II reionization occurred in the range $3 \leq z \leq 4$ consistent with observations.

In this paper we present a simulation which is similar in spirit to SAH, but with several important differences. We also postprocess a series of snapshots from a hydrodynamic cosmological simulation with a radiative transfer code, however we keep track of the photoheating of the IGM

as expanding He III spheres percolate and eventually merge. Our hydrodynamic simulation was performed on an Eulerian grid of 512^3 cells versus SAH’s 224^3 in the same volume, giving us ~ 12 times the mass resolution and ~ 2.3 times the spatial resolution in the low density IGM. We have also separated the effects of stellar and quasar populations of the ionization evolution of the IGM differently from SAH. Our hydrodynamic simulation computes the ionization of H I and He I due to stellar sources only using the homogeneous UVB of Haardt & Madau (2001) arising from galaxies ”GAL”. In the post-processing step, quasars are treated as point sources, which ionize He II to He III. Although our radiative transfer scheme is based on completely different spatial and angular discretizations as SAH, the important difference for the purpose of this paper is that we solve the RT equation at three frequencies $h\nu=4, 8$ and 16 Ryd in order to evaluate, albeit crudely, the local He II photoheating rate taking the processed QSO spectrum into account.

The outline of this paper is as follows. In §2 we describe the cosmological realization for the hydrodynamic simulation of homogeneous H I and He I reionization described in §3. In §2 we also introduce some physical concepts relating to late He II reionization and also describe our treatment of quasars in the simulation volume. In §4 we describe our method for simulating inhomogeneous He II reionization. In §4.1 our radiative transfer scheme is detailed, in §4.2 we present our single species ionization model for He II, and in §4.3 we present results in terms of globally integrated quantities. Since we have split the calculation into two phases, the homogeneous reionization of H I and He I, followed by the inhomogeneous reionization of He II, our calculation is not fully self-consistent. Although we keep track of the late reheating, we do not modify the underlying density fields nor do we alter temperature-dependent recombination rates, which will affect the detailed ionization state of the gas. In §5 we present an analysis of our main result, which is the late reheating of the IGM due to inhomogeneous He II reionization, as well as the importance of neglecting these coupling effects. We show that these effects, while present, are small, and do not seriously undermine our estimate of the reheating. In §6 we present observational signatures of He II reionization based on synthetic H I and He II Ly α absorption line spectra derived from our simulation. In §7 we summarize our main results and conclude. In a series of appendices we derive the rate equation for species fraction in an expanding universe (Appendix A), provide more detail on the affect of neglecting He II photoheating on the ionization state of the gas (Appendix B), and document the reaction rate coefficients we use (Appendix C).

2. Simulations

2.1. Cosmic Realization

In this work, we present the results from post-processing the redshift evolution of a cosmic realization computed with the Eulerian cosmological hydrodynamic code Enzo (Bryan & Norman 1997; Norman & Bryan 1999; O’Shea et al. 2004). The box of size $67h^{-1}$ Mpc comoving was evolved in a flat ($\Omega = 1$) Λ CDM cosmology on a unigrid mesh of 512^3 grid cells and 512^3 dark

matter particles from $z=99$ to $z \simeq 2$. We used the initial power spectrum of matter fluctuations by Eisenstein & Hu (1999) to initialize the calculation which was then computed forward under the Zel’dovich approximation (Bertschinger & Gelb 1991). Our choice of cosmological parameters is $\sigma_8 = 0.8$, $\Omega_\Lambda = 0.7$, $\Omega_b = 0.04$, $n_s = 1$ with a present day Hubble constant of $h = 0.67$ in units of 100 km/s/Mpc. With these parameters our cosmic realization has a mesh resolution of $130h^{-1} \simeq 200$ kpc within the 100 Mpc cube, and $\simeq 1.6h^{-1} \times 10^8 M_\odot$ dark matter particle mass. In Figure (1) we show a volumetric rendering of the cosmic gas distribution as mapped by the baryon overdensity in our simulation at $z=2.6$.

One of the fundamental simplifications used here, which places limits on the validity of our results is that the ionization of H I and He I are treated entirely differently than He II. The motivation is that of numerical simplicity and calculation speed. From the IGM cosmological evolution standpoint, hydrogen and neutral helium are believed to be globally ionized at an earlier cosmic epoch than He II. In the simulation discussed here, the photo-ionization/heating rates of H I and He I are computed self-consistently during the hydrodynamical calculation in the optically thin regime. The premise of our argument is that, if one adopts a picture where neutral hydrogen and neutral helium reionization is completed by $z \simeq 6$, such species will have large ionization fractions by the time He II reionization occurs, which theoretical models and observations place at $z \simeq 3 - 2$.

The reionization of the H I /He I species is achieved by the evolving uniform metagalactic flux due to stellar sources as computed in Haardt & Madau (2001). The uniform ultra-violet background photo-ionizes and photo-heats the IGM, however it is prevented by hand to radiatively alter the He II abundance. We do so by suppressing the ionization/heating rates in Enzo that control the $\text{He II} \leftrightarrow \text{He III}$ chemistry. The latter is computed separately by our inhomogeneous point-source distribution of QSOs which is discussed in §2.3.

The initial calculation represents an undisturbed cosmological ensemble of gas fields ionized by a distributed galaxy population. The local QSO component then acts as a perturbation in the amplitude of the radiative energy that further ionizes and photoheats the diffuse IGM. The end result is that the He II reionization proceeds, under the limitations discussed above, via the mergers of individual He III I-fronts during the cosmic epoch that spans the redshift interval $z = 6 - 2$.

2.2. Why Late He II reionization

In this section we introduce some definitions and basic results related to He II reionization that we will refer to later on. The softness parameter of the cosmic radiation is defined as $S = \frac{\Gamma_{HI}}{\Gamma_{HeII}}$. In the optical thin limit under a single power law profile for the radiation spectrum, $J_\nu = J_{912}(\frac{\nu}{\nu_{912}})^{-\alpha_q}$, where J_{912} denotes the volume averaged mean intensity at the hydrogen ionization threshold, we can estimate the photoionization rates to be $\Gamma_{HI} \equiv \Gamma_1 = \frac{4\pi J_{912} \sigma_{HI}^o}{h} \frac{1}{1+\alpha_q}$ and $\Gamma_{HeII} \equiv \Gamma_2 = \frac{4\pi J_{912} \sigma_{HeII}^o}{h} \frac{1}{1+\alpha_q} 4^{-\alpha_q}$. Dividing the last two relations yields an estimate for the softness parameter in the optical thin limit equal to $S = 4^{1+\alpha_q}$. Therefore, the ability of a background radiation

field to ionize the H I and He II species depends on the spectral slope. A soft radiation field would have large spectral slope and would primarily favor hydrogen ionization. He II ionization therefore requires a hard ionizing spectrum.

The available sources of radiation at redshifts $z \leq 10$ are of two types. Stellar sources, associated with radiation from galaxies forming in the cosmic medium at such redshifts, have large softness parameter values of $S_{stellar} \sim 4 \times 10^3$. QSOs on the other hand, have much smaller softness parameter values of $S_{QSO} \sim 50$ which makes them ideal for He II ionization. However, the number density of QSOs, as measured by observations sharply rises in the interval $6 > z > 3$ and reaches a peak at about $z \approx 3$ (Pei 1995). The highest redshift QSO observed to date is at $z_{em} = 6.56$ (Hu, Cowie & McMahon 2002). Direct observations of QSO in Ly α spectra are very difficult because of the hydrogen Gunn-Peterson effect, the optical depth manifestation of hydrogen neutrality at high redshifts (Fan, Carilli & Keating 2006). This suggests that either the quasars have a well established population by $z \approx 6$ but nevertheless obscured by the large optical depth or that their formation began at that epoch. However, when their emissivity is computed at redshifts just past the Gunn-Peterson trough, their numbers and spectrum shape is insufficient to produce the hydrogen reionization thought to be primarily achieved by a stellar component in the UVB which ionizes hydrogen and neutral helium to the singly ionized state. Because the stellar component of the radiation background is not an efficient He II ionizer, He II reionization is expected to occur later; at times when a sufficient number hard photons becomes available.

The Gunn-Peterson optical depth of He II for a uniform IGM can be expressed in the same way as the corresponding H I and that leads to the ratio $\frac{\tau_{HeII}(z)}{\tau_{HI}(z)} = \frac{n_{HeII} \sigma_{HeII}}{n_{HI} \sigma_{HI}} = \frac{1}{4} \frac{n_{HeII}}{n_{HI}}$. The ratio of optical depths is known as the R-factor and is used in observations to measure the relative properties between the He II and H I Ly α forest spectra. Observations find that in transmission spectra longward of quasars seen at emission redshifts $z \sim 3$ typically measure values of the R-factor between $R \approx 10 - 100$ within $\delta z \sim 0.5$ (Reimers et al. 1997; Heap et al. 2000; Kriss et al. 2001). This suggests the presence of a HeII Gunn-Peterson trough at redshifts $z \gtrsim 2.5$. In the optical thin limit the R-factor and the softness parameter relation can be derived.

In ionization equilibrium the ratio of n_{HeII}/n_{HI} can be computed if we assume that the higher ionization states of both species (He III, H II) dominate. In that case, for hydrogen we get $\chi_1 \Gamma_1 = n_e \alpha_1 (1 - \chi_1)$ where $\chi_1 = n_{HI}/n_H$ and α_1 is H II the recombination coefficient. Similarly for He II we can also write $\psi_2 \Gamma_2 = n_e \alpha_2 (1 - \psi_2)$, where $\psi_2 = n_{HeII}/n_{He}$ and α_2 is the He II recombination coefficient. The above two relations yield $\chi_1/\psi_2 \simeq \frac{\Gamma_2 \alpha_1}{\Gamma_1 \alpha_2}$, for $\chi_1 \ll 1$ and $\psi_2 \ll 1$. The last equation allows for the determination of the ratio $n_{HI}/n_{HeII} = \frac{\chi_1 n_H}{\psi_2 n_{He}} \simeq 12 \times \frac{\Gamma_2 \alpha_1}{\Gamma_1 \alpha_2}$. Therefore, for $\frac{\alpha_2}{\alpha_1} \sim 5$ (at $T \approx 10^4$ K) the ratio of number densities becomes $\frac{n_{HeII}}{n_{HI}} \simeq \frac{5}{12} S$. From the last relation it follows that $R \simeq 0.1 S$. For $S \simeq 4 \times 10^3$ (stellar radiation) the relation predicts $R \simeq 400$. Similarly for quasar radiation, with $S \simeq 50$, $R \simeq 5$. In addition, we can compute that since the quantity $n_e \alpha(T)/\Gamma = \tau^{ion}/\tau^{rec}$, the ratio of the ionization to recombination time scales, $\frac{\tau_{HeII}^{ion}}{\tau_{HeII}^{rec}} = 5S \frac{\tau_{HI}^{ion}}{\tau_{HI}^{rec}}$

Typical softness parameter values $S \geq 100$ then yield $\frac{\tau_{HeII}^{ion}}{\tau_{HeII}^{rec}} \geq 5 \times 10^2 \frac{\tau_{HI}^{ion}}{\tau_{HI}^{rec}}$. The last relation

shows that, due to the larger recombination coefficient and the fewer number of photons available for ionization, it is more difficult to ionize He II compared to H I . The shorter (longer) recombination (ionization) time scale effectively restricts He II reionization to take place at a slower rate.

Large values in the R-factor is suggestive of large optical depths in He II and/or small optical depths in neutral hydrogen. Comparable optical depths at late redshifts, which correlate to small cosmic neutral hydrogen fraction and therefore small cosmic fraction in He II , yield small values for the R-factor. The observations can therefore infer a range in the observed softness parameter from measuring the ratio of optical depths in the He II and H I line forest. The observed range of $R=10-100$ consequently suggests that $S=100-1000$ between $z=2-3$ although the upper limit is an overestimate because we assumed $\psi_2 \ll 1$. Because such observed values are sampled in transmission spectra that probe the ionization phase transition of He II to He III , we can infer that at that epoch the galaxy dominated ultraviolet background is gradually being replaced by a quasar dominated type.

In §6, we show that the R-factor evolves with redshift from large to small values as it is computed in transmission through the computational volume. The quantity that is actually computed is the η parameter defined as the column density ratio between He II and H I , $\eta = \frac{N_{HeII}}{N_{HI}}$. The R-factor evolution and value follows directly as $R = \frac{\eta}{4}$. The gradual evolution of the R-factor and η parameter from large values is indicative of the cosmic evolution of the softness parameter from a stellar to a quasar dominated type.

2.3. Quasar Placement and Evolution Pre-processing

For the quasar placement and evolution in the simulation we use the quasar luminosity function by Pei et al. (1995), shown in Equation (2). This luminosity function was also used by Haardt & Madau (1996,2001) to derive the quasar emissivity and the volume average photoionization and heating rates used in the simulation for every species other than He II .

$$\phi(L, z) = \frac{\phi_*/L_*(z)}{[L/L_*(z)]^{\beta_1} + [L/L_*(z)]^{\beta_2}} \quad (2)$$

$$L_*(z) = L_*(0)(1+z)^{\alpha_q-1} \frac{e^{\zeta z}(1+e^{\xi z_*})}{e^{\xi z} + e^{\xi z_*}}$$

Our first requirement is the placement of a single QSO in the computational volume at $z=6.5$. The redshift is for all practical purposes a matter of choice, since there is no accurate prediction of when the first QSO appears in the universe. We adopt a scenario where quasars become visible in observations after the epoch of hydrogen reionization is completed by $z \simeq 6.5$ due a soft component in the ultra-violet background most likely associated with dwarf galaxy formation. In addition, we are constrained by the mass resolution of our simulation, which cannot resolve halos smaller than

$\simeq 5 \times 10^9 M_\odot$. Therefore, quasar point sources have to be placed in the centers of halos above this cutoff. We do so by identifying the evolution of a list of halo centers through the computational volume from $z = 6.5$ to $z = 2$. The number of quasars per redshift interval is determined by the luminosity function in Equation (2) and the functional form of the mass-halo to quasar luminosity relation.

We assume an intrinsic quasar spectrum $J_\nu = J_{912}(\frac{\nu}{\nu_{912}})^{-\alpha_q}$ for the LyC part of the spectrum with a spectral index $\alpha_q = 1.8$. Therefore, the number flux of emitted LyC photons, in *photons/s/cm²*, is then $\dot{n}_{ph} = \frac{4\pi J_{912}}{h} \int_1^\infty \frac{\epsilon^{-\alpha_q}}{\epsilon} d\epsilon$. In this relation, $\epsilon = \frac{h\nu}{h\nu_{912}}$. The integration yields $\dot{n}_{ph} = \frac{4\pi J_{912}}{h\alpha_q}$. Similarly the LyC energy flux is $l_{LyC} = \frac{4\pi\nu_{912}J_{912}}{\alpha_q - 1}$, which yields $l_{LyC} = (h\nu_{912})\dot{n}_{ph}\frac{\alpha_q - 1}{\alpha_q} \Rightarrow L_1 = (h\nu_{912})\dot{N}_{ph}\frac{\alpha_q - 1}{\alpha_q}$. In the last equation, L_1 and \dot{N}_{ph} represent the total LyC luminosity (ergs/s) and emitted photon rate (photons/s) respectively per point source (QSO) above the H I ionization threshold of 1 Ryd (13.6 eV). This allows for a parametrization of the emitted ionizing flux based on the number of LyC photons rather than energy. The motivation is entirely for consistency with the photon-conserving schemes in simulating reionization (Abel & Haehnelt 1999; Sokasian, Abel & Haehnelt 2001, 2002; Ciardi et al. 2003; Whalen, Abel & Norman 2004). The total luminosity for the He II ionizing radiation above 4 Ryd (54.4 eV) is then obtained through $L_4 = 4^{-(\alpha_q + 1)} \times L_1$. The luminosity of each source is determined by the dark matter mass of the halo that initially creates it. For a dark matter halo of mass M_{halo} we put in a UV source emitting $\dot{N}_{ph} = 10^{51} \times \frac{M_{halo}}{10^8}$ H I ionizing photons/s. This is equivalent to placing a $\dot{N}_{ph} = 10^{51}$ *ph/s* mini-quasar inside a $10^8 M_\odot$ dark matter halo which is the prescription used in Abel & Haehnelt (1999). Sokasian et al. (2001) investigated an array of QSO placement methods in the computational volume and found that the results are largely insensitive to the choice. We adopt the linear relation for convenience. In this work, the most massive halo computed at $z=2.5$ has mass $M_{halo} \approx 6 \times 10^{13} M_\odot$. If a QSO source is placed there then it will emit LyC photons at a rate of $\dot{N}_{ph} = 6 \times 10^{56} s^{-1}$. For an input spectrum with slope $\alpha_q = 1.8$ the photon rate corresponds to a LyC luminosity of $L_1 = 2.9 \times 10^{46}$ ergs/s and $L_4 = 6.1 \times 10^{44}$ ergs/s for H I and He II respectively.

The placement of the point sources in the volume is dynamical in nature. The list of dark matter halos is assigned a quasar source with a luminosity value determined by our phenomenological prescription. The location of the quasar from that point on is locked to the position of the dark matter particle closest to the center of the halo. The distribution of luminosities is then integrated from the higher value to the smallest up to the point where the average luminosity per unit volume reproduces the distribution fit given by Equation (2) at each redshift. For simplicity, we do not evolve the luminosity in each dark matter halo, which remains the same at initialization. As the luminosity function increases with decreasing redshift additional sources are spawned in the simulation, leading to an overall increase of their numbers. At $z \lesssim 3$ the flattening and subsequent decrease in the luminosity function is modeled by randomly removing point sources from the quasar list. In the right panel of Figure (1) we show the redshift evolution in the number of QSO sources in the volume.

The location each point source is used to compute the 3D distribution of the tensor Eddington

factor (§4.1) which is stored at each cosmic time step. The local value $f_{ij}(\mathbf{x})$ at t^n is an interpolated value between the local values of the two data dumps whose redshifts bound the instantaneous time ($z_1 \leq t^n \leq z_2$). As we will discuss in the next sections, the cosmic evolution of the helium reionization is decoupled from the corresponding hydrogen one. Consequently, the placement of a He II ionizing source on a density peak with a precomputed hydrogen and therefore electron density can yield significant discrepancy between our calculation and a self-consistent one, particularly in close proximity to the source.

3. Homogeneous Hydrogen Ionization

As mentioned above, in the numerical and physical setup of this present work, we treat the ionization of H I and He I separately from He II. The metagalactic flux we use from Haardt & Madau (2001) tabulates the contributions due to galaxies (GAL) and quasars (QSO) separately. In Enzo we have the option of running a simulation with GAL only, QSO only, or GAL+QSO. In a standard optically thin simulation the GAL+QSO UVB would be used. We have carried out such a simulation, hereafter called Simulation A, for comparison with the inhomogeneous reionization simulation. For the latter, we first run a hydro simulation using the GAL UVB to ionize H I and He I. Then He II reionization is accomplished by treating quasars as point sources as detailed in §4. Since our quasar population follows the same luminosity function and intrinsic spectrum as assumed by Haardt & Madau, we are able to compare the homogeneous and inhomogeneous simulations directly. We consider the effect of the $\epsilon \geq 54.4$ eV photon field as a perturbation on the previously ionized gas which affects only the He II \leftrightarrow He III chemistry while the H I and He I ionization states remain unaffected. The treatment is by all measures an approximation that allows the problem to be solved as a single species ionization problem only and therefore it remains conceptually simple. In reality, the ionization of He II has two inter-dependent effects; it releases additionally one electron per He II ionization which in turn, when thermalized, raises the mean temperature of the IGM. These two effects combined would in principle shift the ionization balance of the H I /H II and He I /He II species. However, we show in this section that because by the time this takes place hydrogen and helium have already large ionization fractions the aforementioned effects are small.

Starting with the rate equation for hydrogen and the cosmic mean density, we can safely ignore the collisional contributions and write the chemical balance in the proper frame of reference as follows:

$$\dot{n}_{HI} = -3H(z)n_{HI} - n_{HI}\Gamma_1 + n_en_{HII}\alpha_1(T). \quad (3)$$

In Equation (3), $n_e = n_{HII} + n_{HeI} + 2n_{HeII}$, Γ_1 is the integrated H I photoionization rate, and $\alpha_1(T)$ is the radiative recombination coefficient in the H II + $e \rightarrow$ H I + γ reaction and is a function of temperature. In a cosmic medium, $n_{He} = fn_H$, where $f \simeq \frac{1}{12}$ for a mass of fraction

of $\rho_H = 0.75\rho$ and $\rho_{He} = 0.25\rho$ respectively. The He II number density can then be rewritten as $n_{HeII} = n_{He} - n_{HeI} - n_{HeIII}$ which in turn allows the electron density to be expressed as follows:

$$n_e = n_H[\chi_{HII} + \frac{(1 - \chi_{HeI} + \chi_{HeIII})}{12}] \quad (4)$$

Changing slightly the notation, we can rewrite Equation (3) according to Appendix (A) in terms of the ionization fractions $\chi_2 = n_{HII}/n_H$, $\psi_1 = n_{HeI}/n_{He}$, $\psi_2 = n_{HeII}/n_{He}$ and $\psi_3 = n_{HeIII}/n_{He}$ as:

$$\begin{aligned} \dot{\chi}_2 &= \Gamma_1(1 - \chi_2) - \chi_2 n_H \alpha_1(T) [\chi_2 + \frac{1}{12}(1 - \psi_1 + \psi_3)] \Rightarrow \\ \dot{\chi}_2 &\approx \Gamma_1(1 - \chi_2) - \chi_2 n_H \alpha_1(T) [\chi_2 + \frac{1 + \psi_3}{12}] \end{aligned} \quad (5)$$

In the last equation, we assumed that almost all of the helium is highly ionized to the He II state $\psi_1 \rightarrow 0$. In ionization equilibrium ($\dot{\chi}_2 = 0$), after setting $A \equiv (1 + \psi_3)/12$ we can rewrite Equation (5) as $(1 + \frac{\chi_2}{A})\frac{\chi_2}{1 - \chi_2} = \Gamma_1/(A n_H \alpha_1)$. On one hand, the ionization of the He II would increase quantity A due to the increase in the He III abundance. On the other hand, the increased temperature would decrease the recombination coefficient which can be approximated as $\alpha_1 \propto T^{-\beta}$, for temperatures in the range of $T \simeq 10^3 - 10^5$ K and $\beta = 0.51$. The approximation is based on expression fits by Bugress (1964).

Therefore, we will investigate two extreme cases. Case (I) represents zero He III abundance, $\psi_3 \rightarrow 0$ and would correspond to the unperturbed temperature T_I . Case (II) represents a limit of almost full He II ionization, $\psi_3 \rightarrow 1$, that would correspond to a new temperature T_{II} . In both cases, the hydrogen ionization rate is the same because our treatment of the individual QSO sources placement has a distribution that is statistically identical to the global average used for H I and He I ionization. Therefore, we can form the ratio:

$$\frac{(1 + \chi_2^{II}/A_{II})\chi_2^{II}(1 - \chi_2^I)}{(1 + \chi_2^I/A_I)\chi_2^I(1 - \chi_2^{II})} = (\frac{T_{II}}{T_I})^\beta \frac{A_I}{A_{II}} \quad (6)$$

Equation (6) is solved in Appendix (B), for χ_2^{II} in the range of $1 - \chi_2^I = 10^{-6} - 10^{-1}$ and for $A_{II} = 1/6$, $A_I = 1/12$, $T_{II}/T_I = 1.5 - 2$. The ratio of temperatures is based on estimates of the temperature increase due to the photoelectrons injected in the IGM from the ionized He II atoms (Haehnelt & Steinmetz 1998; Abel & Haehnelt 1999) and will be discussed in more detail in §5. The results in the Appendix figures show that when hydrogen is highly ionized then the shift in the ionization balance due to the He II ionization results in a decrease of the neutral hydrogen fraction primarily due to the decrease of the ionized hydrogen's recombination coefficient.

The $\approx 15 - 25\%$ reduction depends on the temperature increase, where the largest increase (a factor of 2) produces the biggest shift. The fractional decrease in the neutral hydrogen fraction is smallest at low fractions of ionized hydrogen. For a typical neutral hydrogen fraction of

$\chi_1 \simeq 10^{-5}$ at post-reionization redshifts, we can then estimate that our treatment (of not updating the hydrogen abundances) would overestimate the neutral hydrogen fraction by about 25% if the gas temperature increase is between 1.5-2 times the non-perturbed value. Consequently, we anticipate an overestimate by the same amount in the optical depth of hydrogen Ly α radiation and an underestimate in the mean transmitted flux. The problem is similar to the one described in Zhang et al. (1997), Bryan et al. (1999) and Jena et al. (2005). An unmodified UVB by Haardt & Madau (1996), applied in those simulations, would not yield an agreement with the observed b-parameter of the Ly α forest. An adjustment by a factor of 1.5-2.0 in the He II photoheating rate was then necessary to match the observed results. Therefore, we caution against a strict interpretation of the resulting hydrogen Ly α forest in the original calculation in which we suppressed the He II photoionization and photoheating processes altogether.

4. Inhomogeneous Helium II Reionization

We compute the inhomogeneous He II reionization due to an evolving distribution of local QSO-type sources by solving for the time and spatial evolution of the ionizing radiation energy density $E_\nu(\mathbf{r}, t)$ as shown in following section. In §4.2 we describe our simplified chemistry model, and in §4.3 we present results. We defer a discussion of late photoheating to §5.

4.1. Radiation Transfer Equation

We consider simulation volumes of box length L much smaller than the horizon scale $L \ll L_H = c/H(z)$. Also, prior to bubble overlap, the time between emission and absorption of a random He II ionizing photon will be much shorter than a Hubble time. In this limit, the cosmological radiative transfer equation reduces to the familiar one (Norman, Paschos & Abel 1998):

$$\frac{1}{c} \frac{\partial I_\nu}{\partial t} + \frac{\hat{n} \cdot \nabla I_\nu}{a} = \eta_\nu - \chi_\nu I_\nu \quad (7)$$

where I_ν is the monochromatic specific intensity, η_ν, χ_ν are emission and extinction coefficients, and ν is the instantaneous, comoving frequency. In equation (7) the gradient is comoving, and hence we divide by the cosmological scale factor a to convert to proper distances. The zeroth and first angular moments of equation (7) yield

$$\frac{\partial E_\nu}{\partial t} + \frac{1}{a} \nabla \cdot \mathbf{F}_\nu = \epsilon_\nu - ck_\nu E_\nu \quad (8)$$

and

$$\frac{1}{c^2} \frac{\partial \mathbf{F}_\nu}{\partial t} + \frac{1}{a} \nabla \cdot \mathbf{P}_\nu = -\frac{1}{c} k_\nu \mathbf{F}_\nu, \quad (9)$$

where E_ν, \mathbf{F}_ν and \mathbf{P}_ν are the radiation energy, flux vector, and pressure tensor, respectively. All quantities are measured in the fluid (proper) frame, where $\epsilon_\nu = 4\pi\eta_\nu$ is the emissivity, and k_ν

is the absorption coefficient. The UV photons are scattered by the free electrons and for the range of electron number densities in the IGM (in the redshift interval we are interested in) we can estimate that λ_s (the scattering mean free path) $= \frac{1}{n_e \sigma_{Th}} > L_H$. Therefore, we ignore the scattering coefficient.

The radiation pressure tensor is coupled to the energy density $\mathbf{P}_\nu \rightarrow E_\nu$ in the moment equations through the tensor Eddington factor, $\mathbf{f}_\nu = \frac{\mathbf{P}_\nu}{E_\nu}$. The latter guarantees the correct direction of the flux vector (Mihalas & Mihalas, 1984). It can be shown that the time derivative term in equation (9) is small compared to the rest if we integrate using a timestep long compared to the light crossing time of a computational cell, as we do. Therefore, dropping the time derivative in equation (9) and combining it with equation (8) we get

$$\frac{\partial E_\nu}{\partial t} = \frac{1}{a^2} \nabla \cdot \left[\frac{c}{k_\nu} \nabla \cdot (\mathbf{f}_\nu E_\nu) \right] + \epsilon_\nu - ck_\nu E_\nu \quad (10)$$

where

$$\nabla \cdot (\mathbf{f}_\nu E_\nu) \equiv \frac{\partial}{\partial x_i} (f_\nu^{ij} E_\nu).$$

In Equation (10), ϵ_ν is the spatially discrete monochromatic emissivity at the locations of the emitting sources and $k_\nu = n_{HeII} \sigma_\nu^{HeII}$ is the local opacity, where the functional form of σ_ν^{HeII} is given by Osterbrock (1989) and in Appendix C. Equation 10 can be solved for $E_\nu(\mathbf{r}, t)$ for a given source distribution provided the spatially-dependent Eddington tensor is known. Formally, f_{ij} is obtained from angular quadratures of the specific intensity (e.g., Hayes & Norman 2003). However, we wish to avoid solving the full angle- and frequency-dependent equation of radiative transfer. Instead we employ a geometric closure introduced by Gnedin & Abel (2001) in which we calculate the radiation pressure tensor assuming the medium is optically thin. In this limit

$$P_{ij\nu}(\mathbf{r}) = \frac{1}{4\pi c} \sum_k^N \frac{L_{k\nu}}{|\mathbf{r} - \mathbf{s}_k|^2} \frac{(\hat{n}_i(\mathbf{r} - \mathbf{s}_k))(\hat{n}_j(\mathbf{r} - \mathbf{s}_k))}{|\mathbf{r} - \mathbf{s}_k|^2} \quad (11)$$

where \mathbf{s}_k are the positions of the ionizing sources, and $\hat{n}_{i,j}$ are the direction vectors (basis) at the point \mathbf{r} . Equation 11 describes pure radial streaming radiation from a collection of point sources in a transparent medium. Until He III bubbles begin to overlap, this is an excellent approximation inside the He III regions but a poor one outside. However, since there is very little ionizing radiation in the He II regions, it makes little difference what one chooses for \mathbf{f} . As discussed by Gnedin & Abel, the greatest error is when two bubbles begin to overlap and the two ionizing sources begin to “see one another.” If one source is much more luminous than the other, this can lead to a $\sim 10\%$ error in the expansion rate of the smaller I-front.

To solve Equation (10) we employ a finite volume method by rewriting the zeroth moment equation in a conservative form and integrating over a grid cell. The energy density, emissivity and opacity are zone centered quantities, therefore $\int_{V_g} E_\nu dV = V_g E_\nu$, $\int_{V_g} \epsilon_\nu dV = V_g \epsilon_\nu$, $\int_{V_g} k_\nu dV =$

$V_g k_\nu$, where V_g is the volume of a grid cell and $E_\nu, \epsilon_\nu, k_\nu$ are now understood to be cell averages. Equation (10) then becomes:

$$\frac{\partial E_\nu}{\partial t} + \frac{1}{aV_g} \oint_{cell} \mathbf{F}_\nu \cdot d\mathbf{S}_{cell\ surf} = \epsilon_\nu - ck_\nu E_\nu \quad (12)$$

$$F_\nu^i = -\frac{c}{ak_\nu} \frac{\partial}{\partial x_j} (f_\nu^{ij} E_\nu)$$

Our time-implicit discretization scheme will be discussed in a follow up paper. Briefly, equation (12) is discretized on a uniform cartesian mesh and integrated using backward Euler time differencing. Spatial discretization of the RHS of equation (12) yields a 19-point stencil. The resulting sparse-banded system of linear equations is solved using the stabilized biconjugate gradient (BiCGstab) algorithm implemented in the MGMPPI package¹ developed by the Laboratory for Computational Astrophysics (Bordner 2002).

For this problem, we compute the radiative energy density at three frequency values above the ionization threshold value, E_1, E_2, E_3 , corresponding to photon energies $\epsilon_1 = 4, \epsilon_2 = 2 \times \epsilon_1$ and $\epsilon_3 = 4 \times \epsilon_1$ in Rydberg units ($\epsilon = \frac{h\nu}{h\nu_{912}}$) respectively. The three points plus a fourth one at $\epsilon_4 = 32$ Ryd with $E_4 = E_3(\frac{\epsilon_4}{\epsilon_3})^{-\alpha_q}$, are used to infer the interpolated profile of a 4th degree polynomial $E(\epsilon)/E_1 = \sum_{k=0}^{k=4} c_k(\frac{\epsilon}{4})^{-k}$ between $\epsilon = 4 - 16$ Ryd. At $\epsilon \geq 16$ Ryd, we assume that $E(\epsilon) = E_3(\frac{\epsilon}{\epsilon_3})^{-\alpha_q}$, which follows from the reasonable assumption that at four times the ionization threshold energy, ≈ 0.2 keV already in the soft X-ray energy band, there is little effect in the attenuation of the radiative energy due to opacity. The interpolation is necessary in order to be able to compute the ionization and heating rates which involve an integration in frequency space (photon energy). The use of three frequencies and locally computing c_k bypasses the requirement more many frequency bins or the rewrite of the moment equations in frequency groups. Our motivation is that our calculation does not aim in computing the reprocessing of the radiation field spectrum, but rather in a reasonable and spatially inhomogeneous estimate of the photoionization/heating rates that will give rise to the 3D He II reionization process.

Upon obtaining the solution $E_{1..3}$, E hereafter, we proceed to compute the local ionization and heating rates as described in §4.2. After that point, the coefficients c_k are no longer necessary and are discarded. The obvious advantage of this method is computational speed in the derivation of the photo-ionization/heating rates through an analytical formula. The disadvantage is that the accuracy is as only good as the cubic interpolation scheme. However, we note that our interpolation scheme does a reasonably good job of describing the processed quasar spectrum obtained with the full multifrequency calculation of Abel & Haehnelt (1999). In fact, our choice of frequency points was strongly guided by the inset spectra in their Figure 1.

The distribution of local sources determine the point source emissivity (source function) and the 3D distribution of the Eddington factor. Because in our numerical setup all sources emit radiation

¹lca.ucsd.edu/portal/software/mgmpipi

with identical spectral slope α_q , the calculation of the Eddington tensor via equation (11) yields a quantity that does not depend on frequency ($f_\nu^{ij} \equiv f^{ij}$). The pre-processing involves keeping track of the sources position and luminosity during the calculation and updating the Eddington factor functional form and emissivity source function at the beginning of each data dump calculation. The Eddington factor is initialized at $f_{source}^{ij} = 1/3\delta^{ij}$ within each grid cell containing a source. Between time steps, assumed to be the redshift interval between the data dumps ($\delta z = 0.1$), we solve for the $E(\mathbf{r}, t_n)$ which we use to update the He II photo-ionization rate Γ_2^{rad} described in §4.2. The photo-ionization rates are then used to compute the next time-step for solving the transfer equation. Because the latter is solved implicitly, the solution is not sensitive to any particular choice of the time-step, beyond obvious concerns of numerical convergence.

4.2. Chemistry Implementation

Our simple single species chemistry determines the time step of the evolution. We update the ionization fraction $\psi_3(\mathbf{x}, t) = \frac{n_{HeIII}}{n_{He}}$ through the rate equation:

$$\dot{n}_{HeIII} = -3H(z)n_{HeIII} + n_{HeII}\Gamma_2 - n_en_{HeIII}\alpha_2(T) \quad (13)$$

In Equation (13), $\Gamma_2 = \Gamma_2^{rad} + \Gamma_2^{col}$ is the sum of the radiative and collisional ionization rates. The collisional ionization is due to collisions of the He II ion with electrons, $HeII + e \rightarrow HeIII + 2e$, and therefore is proportional to the electron density n_e . The collisional ionization rate per electron Γ_2^{col}/n_e is a function of the gas temperature. An analytic fit to the temperature dependence is provided in Appendix C where we also provide the functional form for the recombination coefficient (both quantities are measured in cm^3s^{-1}). The photoionization rate per baryon is then given by the equation (Osterbrock 1989) $\Gamma_2^{rad} \equiv \int_{\nu_{224}}^{\infty} c \frac{E_\nu}{h\nu} \sigma_\nu^{HeII} d\nu$. Because we find a parametric fit of the energy density in frequency space the photoionization can be directly computed as follows. $\Gamma_2^{rad} = \frac{c}{\sigma_{224}^{HeII}} h [E_3 \frac{4^3}{\alpha_q + 3} + E_1 \sum_{k=0}^4 \frac{c_k}{k+3} (1 - 4^{-(k+3)})]$, where we approximate the ionization cross section with the power law $\sigma_\epsilon = \sigma_{224}^{HeII} (\frac{\epsilon}{4})^{-3}$.

To determine the time-step δt^n for the advancement of the radiation solution between t^n and t^{n+1} , we follow the procedure below. We collect the photoionization time-scales, $\tau_{chem} = (\Gamma_2^{rad})^{-1}$, from grid cells that lie in the vicinity of the ionization front and then calculate δt through $\delta t = \max(\tau_{chem}, \tau_{lc})$, where τ_{lc} is the cell light crossing time-scale, $\tau_{lc} = \delta x c^{-1}$. Cells close the I-front interface are “captured” by the criterion $\frac{\Delta n_{HeIII}}{n_{HeIII}}(t^n) \gtrsim 0.1$. Comparison between the light-crossing and chemical time scales is necessary in the initial moments of the evolution, because in proximity to the source the I-front propagates close to the speed of the light. Evolving the energy density with the light-crossing time-scale constrains the I-front expansion to subluminal speeds. In addition, the use of a chemical time-scale close to the source would yield very small time-steps, due to the large number of photons, that would in turn slow down the overall calculation.

Before we proceed, we need to make the following very important clarification. In this

work, we do not consider contributions to the radiative energy density by He II recombinations despite including them in the update of the He II abundance. The significance of the contributing He II recombinations to the energy density are important when a consistent ionization calculation of all species is performed. In that case, radiative recombinations to energies $\epsilon < 54.4$ eV would contribute to the ionization balance of hydrogen and helium. However, these species are already at high ionization fractions and therefore such contributions are not expected to have a significant effect in our scheme. In a consistent calculation, the photon flux from the central source creates a concentric set of Strömgen regions where the ionized hydrogen and helium II extend ahead of the corresponding helium III volume. In such a scheme, recombinations at the He III ionization front yield photons with energies $\epsilon < 54.4$ eV which can freely propagate forward through the already ionized He I and H I and assist in the advancement of the He II and H II fronts respectively. In our setup, there are no He II and H II Strömgen regions, only He III ones. Therefore, the photon flux from recombinations on the He III I-fronts are ignored and we only consider the chemical effects resulting from the attenuation and percolation of the individual He II ionizing flux.

However, recombinations are included in the abundance update primarily because it can be an important effect for the diffuse helium in proximity to a local source that shut off. The lack of direct photons could lead to a rapid recombination of the He III bubble, if no additional radiative flux reaches that region from another QSO source. Equation (13) can then be rewritten as follows.

$$\dot{\psi}_3 = \frac{(1 - \psi_3)}{\tau_2^{ion}} - \frac{\psi_3}{\tau_2^{rec}} \quad (14)$$

In Equation (14), $\tau_2^{ion} = (\Gamma_2)^{-1}$ is total ionization time scale and $\tau_2^{rec} = (\alpha_2(T)n_e)^{-1}$ is the local He III recombination time scale and Γ_2 is the sum of all ionization processes that lead to the forward reaction $\text{He II} \rightarrow \text{He III}$ and we have assumed $\psi_1 \approx 0$. These processes in our scheme involve the combination of the direct photoionizations from the QSO sources Γ_2^{rad} and collisional ionization $\Gamma^{col} = n_e k^{col}(T)$. We integrate equation 14 using backward Euler time differencing where all source terms are computed at the advance time t^{n+1} .

$$\psi_3^{n+1} = \frac{\psi_3^n + \delta t^n / (\tau_2^{ion})^{n+1}}{1 + \delta t^n [\frac{1}{(\tau_2^{ion})^{n+1}} + \frac{1}{(\tau_2^{rec})^{n+1}}]} \quad (15)$$

In Equation (15), only the photoionization rate Γ_2^{rad} is available at the advanced time. Therefore, we are forced to initialize the abundance update by computing $(\frac{1}{\tau_2^{ion}})^{n+1} \simeq \frac{1}{(\Gamma_2^{rad})^{n+1} + n_e^n (k^{col}(T))^n}$ and substitute $(\frac{1}{\tau_2^{rec}})^{n+1} \rightarrow (\frac{1}{\tau_2^{rec}})^n$. However, upon obtaining the He III number density at t^{n+1} , $n_{HeIII} = \psi_3^{n+1} n_{He}$ we can update the electron density at t^{n+1} and insert it back in Equation (15). We therefore can improve upon the original estimate by iterating Equation (15) until $\frac{\Delta n_e}{n_e} \leq 0.1$. Unfortunately, our methodology of updating the temperature, as described in §5, is crude and is not used in the iterative scheme. The local helium number density at any time is computed from the gas density as $n_{He} = \frac{\rho_{He}}{4m_H} \simeq \frac{\rho}{16m_H}$. The electron density is given by the charge conservation equation $n_e = n_{HII} + n_{HeII} + 2n_{HeIII}$. Our calculation assumes no change in the ionized hydrogen density between the value in the original simulation (o), and the post-processed value (1).

Therefore, $n_e^1 - n_e^o = (n_{HeII}^1 - n_{HeII}^o) + 2(n_{HeIII}^1 - n_{HeIII}^o) = (n_{HeIII}^1 - n_{HeIII}^o)$. which allows the calculation of the local electron density at any time from $n_e = n_e^o + (n_{HeIII} - n_{HeIII}^o)$.

4.3. Results

In Figure (2), we show volumetric renderings of $n_{HeIII}(\mathbf{r}, z)$ at two redshift instances. The 3D visualization shows the expanding ionized bubbles filling up the cosmic volume due to the combined effect of the radiative energy transport and sources being turned on at different parts of the volume at later redshifts. Individual bubbles of He III may stagnate as they reach their Strömgren radii due to recombinations. However, overall the volume filling factor (VFF) of He III increases as more quasars are placed in the computational volume and the percolation between the I-fronts increases the mean free path of the ionizing photon flux. In left panel of Figure (3), we show a slice through the cosmic volume at $z = 2.6$ of the He II, He III density distributions. Ionized regions have percolated through the cosmic medium to “open up” the IGM to $\gtrsim 54.4$ eV radiation, effectively completing He II reionization by such redshifts. In the right panel of Figure (3), we show the redshift evolution of the VFF, as measured by the fraction of the grid cells with ionized helium at He III abundance of $\psi_3 \geq 10^{-5}$. As the ionized regions begin to merge, assisted by the increase in the QSO number density, the VFF(z) rapidly increases, leading to a value of $> 68\%$ at $z \leq 2.8$. The redshift of significant merging, which we define as $VFF \approx 0.90$ is achieved by $z \approx 2.5$ where we point to a statistical global He II reionization. This redshift value compares well with the observed determination by Kriss et al. (2001). The solid line in the VFF evolution figure is a spline fit through the computed data ($\delta z = 0.1$). For reference, we include the derived values every $\delta z = 0.5$, along with the error estimates based on the location uncertainty of the I-front. The uncertainty is simply due to the fact that computing the radiative energy density in the zone centers yields no information on the profile of the field across the grid cell. Therefore, we assigned an error estimate in the ionized volume fraction equal $(\frac{\delta x}{2})^3/V$, where δx is the grid resolution and V is the volume of the computational box. The evolution of the VFF shows a rapid increase in He III at redshifts $z \lesssim 4$, following an earlier epoch of apparent stagnation.

An alternative way to illustrate He II reionization is to plot the redshift evolution of the volume averaged abundance fraction. In the left panel of Figure (4), we show that the mean mass fraction in He II ρ_{HeII}/ρ , drops significantly at $z \lesssim 4$. For reference, we also show the mean fraction in H I ρ_{HI}/ρ , undergoes a steep drop at $z \simeq 6.5$ and continues to decrease under a smooth redshift profile, the properties of which are discussed in Paschos & Norman (2005). One notable difference in examining the two evolution profiles emerges between the slopes of the two curves. Beyond the fundamental differences in the ionization calculation of the two species, the result shown in Figure (4) shows that the He II reionization epoch is much more extended than that of H I. A rapid drop in the H I fraction occurs between $z = 7 - 6.5$ (Razoumov et al. 2002; Paschos & Norman 2005). In that redshift range the mean H I mass fraction drops by 4 dex. By visual inspection of the mean fraction in He II from Figure (4) we can determine that it drops by ~ 2 dex

between $z = 3.5 - 2.5$. When the difference in the redshift interval is converted to cosmic time it yields that a similar drop in the mass fraction takes approximately eight times longer to occur in the case of He II when compared to H I. This is consistent with the conclusion reached in §2.2, where the latency in the He II reionization is attributed to higher recombination time scales and less available ionizing photons per baryon for a stellar dominating UV background.

In the right panel of Figure (4), we plot the He II mass fraction versus the local overdensity by logarithmically binning the latter quantity and computing the mean and median He II from the cells with gas density within the bin. Such a graph is intended to show the trend between the two quantities. For reference, we plot the trend between the two quantities from a standard cosmological simulation, where all ionizations are computed self-consistently due a uniform UV background in the optically thin approximation.

The simulation is terminated at $z \simeq 2.5$ at $VFF \simeq 0.9$. The reason for suspending the calculation is that when the cosmic volume is effectively transparent to the ionizing radiation, the assumptions underlying equation (7) no longer apply. Specifically, free streaming photons may cross the volume unimpeded by absorption and their mean free path can become comparable to the size of the horizon. The latter effect requires keeping the cosmological dilution term in Equation (12), which was ignored. From the numerical perspective, solving a parabolic equation when the conditions call for a hyperbolic one, can create local superluminal speeds of the ionizing front if the chemical time scale becomes smaller than the cell light crossing time. Concluding the calculation at the end of the opaque phase of He II still addresses the main question investigated in this work; what is the primary mechanism that leads to the He II reionization. We conclude, that a rising population of QSO sources, assisted by the gas dilution due to cosmic expansion, clumpiness due to structure formation and the pre-ionization of neutral hydrogen which allows for the almost exclusive usage of the He II ionizing radiation are a set of physical conditions that reproduce the epoch of He II reionization by redshifts $z \leq 2.5$.

5. Late Heating due to He II Reionization

5.1. Physical Considerations

Photoionization of He II at an epoch later than that of H I releases an additional one photoelectron per ionization. We can estimate the mean energy of such electrons due to absorption of photons with energies $\geq 54.4 \text{ eV} \equiv 4 \text{ Ryd}$ by He II and compare it to the value obtained in the case of $\geq 13.6 \text{ eV} \equiv 1 \text{ Ryd}$ absorption by H I atoms. For simplicity, we will ignore the geometric attenuation and optical depth effects in the radiative flux due to local sources and gas opacity and assume that the local mean intensity of the radiation is the same as the emitted, with a spectrum $J_\epsilon = J_{912}\epsilon^{-\alpha_q}$. As before, in this notation $\epsilon = \frac{h\nu}{h\nu_{912}}$. The photo-heating rate, in ergs/s, due to electrons ejected from He II atoms, can then be computed from $\bar{G}_{HeII} = \nu_{912} \int_4^\infty (4\pi J_\epsilon / \epsilon)(\epsilon - 4)\sigma_\epsilon d\epsilon$. Substituting for the power law of the mean intensity, for $\sigma_\epsilon = \sigma_{HeII}^o 4^3 \epsilon^{-3}$ we get $\bar{G}_{HeII} = \frac{4\pi\nu_{912}J_{912}\sigma_{HeII}^o 4^{1-\alpha_q}}{(\alpha_q+2)(\alpha_q+3)}$.

In a similar manner, we can derive $\bar{G}_{HI} = \frac{4\pi\nu_{912}J_{912}\sigma_{HI}^o}{(\alpha_q+2)(\alpha_q+3)}$. If the sources responsible for the He II and H I ionization are the same then the J_{912} amplitude and the α_q spectral slope are identical in both equations which allows for the derivation of the following ratio:

$$\frac{\bar{G}_{HeII}}{\bar{G}_{HI}} = \frac{\sigma_{HeII}^o}{\sigma_{HI}^o} 4^{1-\alpha_q} \quad (16)$$

Substituting for $\sigma_{HeII}^o = \frac{\sigma_{HI}^o}{4}$ we get $\frac{\bar{G}_{HeII}}{\bar{G}_{HI}} = 4^{-\alpha_q}$. The total photoheating rate per unit volume is proportional to the number density of the absorbers which yields the ratio between He II and H I photoheating rates to be $G_{HeII}/G_{HI} = \frac{n_{HeII}}{n_{HI}} 4^{-\alpha_q}$. The ratio of number densities is estimated in §2.2 to be $n_{HeII}/n_{HI} = \frac{5}{12}S$, where S is the softness parameter. The ratio of the photoheating rates then becomes $G_{HeII}/G_{HI} = \frac{5}{12}S4^{-\alpha_q} \simeq \frac{5}{12}4^{\alpha_q+1}4^{-\alpha_q} = 5/3$. The latter factor is indicative of the degree of temperature increase due to the thermalization of the photoelectrons ejected by He II ionizations when compared to the temperature inferred by H I ionization alone.

In deriving the above value, we made the assumption that hydrogen and singly ionized helium are photoionized simultaneously by the same ultraviolet field. The effects of distinct ionization epochs can however be modeled in the above relation if we adopt the scenario of hydrogen ionization by a soft radiation background ($\alpha^{(2)} \sim 5$) and of He II ionization by a hard one ($\alpha^{(1)} \sim 1.5$). At a point in time when the populations of galaxies and QSOs have the same energy output at the LyC limit ($z \simeq 4$), we can derive an estimate of the photoheating rates ratio to be $\frac{G_{HeII}}{G_{HI}} = \frac{5}{3} \frac{(\alpha_q^{(2)}+2)}{(\alpha_q^{(1)}+2)} \simeq \frac{10}{3}$ for $\alpha_q^{(1)} = 1.5$ and for $\alpha_q^{(2)} = 5$. In conclusion, the thermalization of the photoelectron in the $HeII + \gamma \rightarrow HeIII + e^-$ reaction can be an important determinant of the intergalactic medium temperature.

Photoionization models based on hydrogen ionization alone predict a temperature of the intergalactic medium of $T_{IGM} \approx 1.2 \times 10^4$ K. However, Ly α forest observations yield lines with median broadening widths of $b = 26 - 36$ km/s (Carswell et al. 1987, 1989; Zhang et al. 1997; Davé et al. 1997) in the intermediate redshift range of $z=2-4$. Because the thermal and differential Hubble flow components in the total H I line broadening are of the same order of magnitude (Zhang et al., 1998; Aguirre, 2002), one can infer a thermal width range in the H I Ly α forest between $b_{th} = 13 - 18$ km/s. The effects of the peculiar velocity can be ignored if the focus is at densities close to the cosmic mean. This value range in b_{th} would require the temperature in the intergalactic medium to be $T_{IGM} = 20,000 - 40,000$ K, a factor of $\sim 1.7 - 3.3$ above the temperature inferred by hydrogen photoionization alone. As seen above, such an increase in temperature can be reproduced by the He II ionization photoheating due to a hard ultraviolet spectrum.

5.2. Perturbed Gas Energy Equation

The post-processing of the simulation data dumps involves an update of the local gas temperature by solving for the perturbed temperature in the thermal energy equation. In the simplest approximation, we will assume that the change in the net rate of the cell thermal energy density is due to the balance between the heating by the ejected photoelectrons from He II ions and the He III recombination cooling, $\frac{1}{\gamma-1} \frac{k\rho}{\mu m_p} \Delta \frac{\delta T}{\delta t} = G - \Lambda$, where $\gamma = \frac{5}{3}$ is the gas adiabatic index, ρ the local gas density and μ the mean molecular weight. All quantities have local proper values. In addition, in the notation followed here $G = n_{HeII} G_r$ is the total photoheating rate, measured in $ergs/s/cm^3$, which is the radiative rate $G_r \equiv \bar{G}$ mentioned above. The cooling rate, Λ , is a function of the local gas temperature and density and is equal to $\Lambda \equiv n_e n_{HeIII} L(T)$. L denotes the cooling function due to He III recombinations and is given by $L(T) = 3.48 \times 10^{-26} T^{1/2} T_3^{-0.2} (1 + T_6^{0.7})^{-1}$ in units $ergs\ cm^3/s$ (Cen 1992), where $T_n = T/10^n$.

Recombination He III cooling is only one out of several processes that cool the cosmic gas, the list of which is described in detail in Anninos et al. (1997). The cooling rate coefficients, in parametric fits that depend on the local gas temperature, due to excitation, ionization and recombination of the primary chemical species along with bremsstrahlung and Compton cooling are fully incorporated into the ENZO code. We expect that He III cooling would dominate the cooling processes inside the He III bubbles when compared to the corresponding He II recombination cooling, because the He II abundance is significantly reduced there to fractions $\psi_2 \simeq 10^{-6} - 10^{-3}$. In addition, the He III recombination cooling rate, along with H II recombination, dominate at the low temperatures found in underdense cosmic regions $T \lesssim 10^4$ K over all other types. In a scheme where hydrogen is already almost completely ionized at $\delta \lesssim 1$ ($\chi_2 \approx 1$), but helium is predominately only singly ionized ($\psi_2 \approx 1$) the thermal balance would be controlled by the heating and cooling of the latter species' ionization.

However, our ability to accurately post-process the temperature field in our scheme is limited by the fact that excitation and collisional ionization cooling from processes involving H I, He I and He II species dominate the cooling curves at temperatures $T \gtrsim 10^4$ K, while exhibiting very steep profiles in the temperature range $T \simeq 10^4 - 10^5$ K. An increase in the gas temperature by the photoelectrons ejected in the He II radiative ionization would cause an increase of the cooling coefficients. Combined with the increase in the electron number density this shift in the thermal balance could significantly increase the cooling rate even though the fractional abundances in H I, He I and He II are small. The end result is that, by only including He III recombination cooling in recomputing the gas temperature, we may overestimate the value of the adjusted temperature. This upper limit in the temperature estimate implies that the recombination time-scale in Equation (15) is also an upper estimate and that the overall propagation of the cumulative He III ionization front is faster than in the case of a self-consistent calculation. However, such calculation would require computing the ionization and thermal balance of all species self-consistently and is beyond the scope of this paper. A numerical scheme is under development that will allow us to do this in the near future (Reynolds et al., *in prep*). Therefore, we conclude that the epoch of He II reionization

may be placed at a later redshift than the one we calculated here ($z_{reion} \sim 2.5$) even though we note that such adjustments could be reversed or may not be necessary if the diffuse recombination radiation is added in the calculation. Such radiation would further ionize H I and He I species suppressing their contributions to the cooling curve. That may explain why, even under all of the assumptions and approximations that we allowed and followed in this work, the end result of our predicted redshift evolution of the He II opacity correlates well with observations of the He II Ly α forest as we shall show in §6.

We proceed with further detailing our temperature update method. If $T^{(o)}$ and $T^{(1)}$ denote the cell temperatures before and after the presence of He II ejected photoelectrons, then we approximate the change in the thermal energy equation as follows:

$$\frac{\delta T^{(1)}}{\delta t} \simeq \frac{\delta T^{(o)}}{\delta t} + \frac{(\gamma - 1)m_p\mu^{(1)}}{k\rho}(G^{(1)} - \Lambda^{(1)}) \quad (17)$$

In an explicit, time-discretized form, where the original temperature at time t^n is obtained by interpolation between the logarithm of the local temperature in the two data dumps with redshifts that bound the time evolution ($z_1 \leq t^n \leq z_2$), Equation (17) becomes:

$$T_{n+1}^{(1)} - T_n^{(1)} = T_{n+1}^{(o)} - T_n^{(o)} + (\delta t)_n(\gamma - 1) \frac{1}{k} \left(\frac{m_p\mu}{\rho} \right)^{n+\frac{1}{2}} (n_{HeII}^{n+\frac{1}{2}} G_r^{n+\frac{1}{2}} - n_e^{n+\frac{1}{2}} n_{HeIII}^{n+\frac{1}{2}} L^n) \quad (18)$$

In Equation (18), time-centered quantities are computed as $X^{n+\frac{1}{2}} = 0.5(X^{n+1} + X^n)$ and only for variables that we know their value at the forward time t^{n+1} . Therefore, L is computed at time t^n because it is a function of temperature which is unknown at t^{n+1} . The update in temperature occurs after all principal quantities of E^{n+1} , n_{HeII} , n_{HeIII} and n_e are computed at t^{n+1} by advancing the local solutions at the implicit time-step of the radiation field discussed in §4.2. The quantity $\frac{m_p\mu}{\rho} = \sum n_i$ is equal to total number density of the cosmic species plus electrons and is computed as follows: $\frac{m_p\mu}{\rho} = [\frac{13}{16} \frac{\rho}{m_p} + n_e]^{-1} \simeq [0.9 \cdot 10^{-5} \Omega_b h^2 (1+z)^3 + n_e]^{-1}$, where the expression for n_e was provided in §4.

In an ideal calculation, if a local grid cell is outside the He III bubble at t^n then $T_n^{(1)} = T_n^{(o)}$ and $n_{HeIII}^n \rightarrow 0$. If no direct ionizing radiation reaches that grid cell by t^{n+1} then $n_{HeIII}^{n+1} \rightarrow 0$ and Equation (18) would predict $T_{n+1}^{(1)} = T_{n+1}^{(o)}$. In a cell where thermal equilibrium was reached during the original calculation between t^{n+1} and t^n then during post-processing $T_{n+1}^{(1)} = T_n^{(1)}$ is achieved only when the heating and cooling terms balance out.

A point of concern is that there was no physical reason to suppress the collisional ionization of He II in the original simulation. Even if there are no ionizing sources capable of radiatively ionizing He II, a local temperature of $T \geq 4.64 \cdot 10^4$ K, found in overdense regions, may be enough to

collisionally eject the 54.4 eV bound electron in the He II atom. Consequently, the temperature evolution $T^{(o)}(z)$ includes such an effect and can skew the post-processed evolution $T^{(1)}(z)$. This is evident if we assume that due to collisional ionization in the pre-processed data $n_{HeIII} \neq 0$ and at t^n , $X_n^{(1)} = X_n^{(o)}$. Equation (18) would then predict $T_{n+1}^{(1)} = T_{n+1}^{(o)} + (\delta t)_n W(n_{HeII}^{(o)}, n_{HeIII}^{(o)}, n_e^{(o)}, T^{(o)})$ where $W \equiv (\gamma - 1) \frac{1}{k} (\frac{m_p \mu^o}{\rho})^{n+\frac{1}{2}} \times (-1) n_{e,o}^{n+\frac{1}{2}} n_{HeIII,o}^{n+\frac{1}{2}} L^n(T^{(o)})$

The last equation would unnecessarily recompute the temperature in regions which lack radiative input but have significant collisional rates in $HeII \leftrightarrow HeIII$ and therefore, $n_{HeIII,o} \neq 0$. To account for such discrepancy in the temperature evolution, each updated local temperature is adjusted as $T_{n+1}^{(1)} = T_{n+1}^{(o)} + (\delta t)_n W(n_{HeII}^{(o)}, n_{HeIII}^{(o)}, n_e^{(o)}, T^{(o)})$. Although in doing so we improve upon the temperature evolution, the collisional effect can never fully be readjusted because of interdependency between all of the physical quantities.

5.3. Results

In Figure 5, we show the results of our temperature calculation. In the left panel, we plot the evolution of the mean temperature in overdensities $\log(\delta) = 0 - 1$ (solid curve). Overplotted is the evolution in the original calculation (dashed) to showcase that at $z \lesssim 3.5$ the two profiles deviate. This demonstrates the effect of late He II photoheating due to the rising population of QSO's in the cosmic volume. The overdensity interval was chosen in order to show that He II reionization is a cosmic event that primarily affects the diffuse and mildly overdense IGM where the temperature can get increased by about a factor of 2 at the end of the calculation. One should consider two effects that support this conclusion. In regions of significant overdensity and therefore dark matter potential, gas is heated by the gravitationally controlled free fall compression to temperatures $T \gtrsim 10^5$ K. Therefore, the effects of photoheating due to the photoelectrons ejected by radiative ionizations of He II only result in an insignificant fractional change. In addition, the large electron density and gas density can be a source of large optical depths and radiation trapping due to increased recombination time scales for a modest increase in the temperature. As a result the radiative energy density can significantly drop in such regions which furthermore reduces the efficiency of He II ionization.

The optical depth effects are demonstrated in the right panel of Figure (5), where we show ($z=2.5$) the median temperature vs. density (solid line) in the scatter plot between the two quantities on the simulation grid. We obtain the curve by binning the gas overdensity in logarithmic intervals and computing the median gas temperature within each bin. For reference, the relation in the original calculation is also shown (dashed lines). On the left panel of Figure (6), we plot the ratio between the optically thick optically thin calculations. The dashed lines shows the effect of our postprocessing on the gas temperature. He II photoionization contributes primarily to the gas temperature at the mean and low gas densities. The effect is diminished at higher overdensities where collisional ionization dominates. In addition to comparing to the original calculation we

also compare to a simulation where the chemical species abundances are self-consistently computed during the simulation due to the same homogeneous UV background and in the optically thin limit. The dot-dashed curves on the right panel of Figure (5) and the left panel of Figure (6) trace the temperature density relation in that case and the ratio to our optically thick calculation respectively. We find that our postprocessed temperature is higher by a factor of $\simeq 1.7$ at the cosmic density level when compared to the optically thin calculation with a homogeneous UV background. This is consistent with the analytical approximation between an optical thick and optical calculation derived in Abel & Haehnelt (1999). Finally, we plot on the right panel of Figure (6) the relation between the slope of the equation of state versus the gas overdensity for all three simulations.

In conclusion, the increase in temperature is a manifestation of the additional heating that results from photoelectrons ejected by He II ionizations in the redshift interval that corresponds to the rise in the number density of sources emitting hard radiation. The physical implication is that the late increase in temperature may well be the reason why the galaxy luminosity function decreases at $z \lesssim 4$. A raise in the mean temperature due to the cosmic evolution of QSO sources would increase the Jeans mass threshold by a factor of 2.2-5 if we adapt an average increase in the temperature between 1.7-3 ($M_{\text{jeans}} \propto T^{\frac{3}{2}}$). The latter would in turn suppress the further formation of dwarf galaxies in the cosmic volume. However, we find that, according to the right panel of Figure (5), the fractional increase in local gas temperature is on average not that large at higher overdensities. If we exclude cosmic neighborhoods that are in close proximity to the local UV sources, where the temperature increase is significantly greater due to the high radiative energy density, then in collapsed structures at $\delta \geq 100$ which are increasingly self-shielding, photoheating is not as effective as shock heating due to gravitational collapse. Nonetheless, a firm conclusion on that effect is not possible in this work, due to the very coarse grid resolution that does not adequately resolve the aforementioned structures.

6. Signatures of He II Reionization

6.1. Synthetic Flux Spectra

The updated He II density and gas temperature can be used to study the effects of this inhomogeneous reionization scheme on the transmission of the intergalactic medium transmission in the He II Ly α restframe wavelength. The objective is to compare with the He II transmissivity obtained from analyzing the currently available observed lines of sight. We synthesize spectra of the He II Ly α absorption at the rest wavelength of 304 Å along 300 random lines of sight (LOS). The number of LOS was chosen in order to yield a less than 1% fluctuation to the mean transmitted flux by the end of the calculation.

The synthesis method is described in detail in Zhang et al. (1997). In addition to He II, we also compute the transmitted flux of the corresponding H I forest at the rest wavelength of Ly α 1216 Å. Each velocity pixel registers the local absorption in He II and H I and therefore maps onto

the same grid location for the two redshifted wavelengths. The redshift interval of the spectrum output is set at $\Delta z = 0.2$. In addition to this interval being the redshift output interval of the hydrodynamic simulation it is a long redshift path that minimizes the sightline to sightline variance by forcing the transmission path to cross and wrap through the volume boundaries along the same directional vector about $\frac{\Delta z}{\Delta z_{cube}}$ times. $\Delta z_{cube} = L H(z)/c$ is the linear size of the cube in redshift units where $H(z) = 100h((1+z)^3\Omega_M + \Omega_\Lambda)^{\frac{1}{2}}$ is the Hubble constant at redshift z and $L=100$ Mpc comoving. At $z = 2.5$ and for $h=0.71$ the Hubble constant is $H(z = 2.5) = 249.1$ Mpc/km/s which yields $\Delta z_{cube} = 0.083$ and $\frac{\Delta z}{\Delta z_{cube}} = 2.4$, the number of wraps through the computational volume.

The output from the hydrodynamic simulation is saved every $\delta z_{dump} = 0.2$ and each optical depth integration is computed between two data dumps at z_1 and z_2 . The output spectrum is therefore centered at $0.5 \times (z_1 + z_2)$, where $z_2 = z_1 - \delta z_{dump}$. The input fields are species density (H I and He II), gas temperature and the three peculiar velocity components, all assumed to be frozen in the comoving frame of reference. However, we allow proper evolution along the redshift path of the sightline for the densities ($\propto (1+z)^3$) and velocities ($\propto (1+z)^{-1}$). The spectra are computed along lines of sight that sample the computational volume continuously for $z \leq 6.1$. We do this by restarting the calculation in the new redshift interval from the mesh location where the previous calculation stopped and continue along the same directional vector. The initial point of origin is randomly selected. After the completion of each $\Delta z = 0.2$ segment we can paste all segments together to obtain a continuous transmission line of sight. The latter can then be resampled at intervals centered to suit our analysis.

At redshifts where absorption features can be recognized as blends of individual lines, a deblending algorithm, described in Zhang et al. (1997; 1998) based on fitting lorentzian profiles below a transmission cutoff, can identify such lines and compute properties such as the column density, broadening width (b-parameter) and equivalent width. We must note, that as the opacity of the IGM increases with redshift and the transmission spectrum is dominated by dark regions, the algorithm fails in identifying the lines. Typically, good results are obtained just past the reionization opacity tail which will be the focus in this analysis.

In Figure (7) we show an example sightline of H I (top left panel) and He II (bottom left panel) Ly α transmission at $z=2.5$ and compare with the results from an Enzo simulation that computes abundances self-consistently in the optical thin limit (top and bottom right panels) using a UVB from a mix of evolving quasar and galaxy populations (Haardt & Madau 2001). Both transmission lines are casted from the same initial point and along the same directional vector. We use the updated temperature and the unperturbed neutral hydrogen abundance for calculating the H I transmission spectra. Although there are few visible differences at first glance, the H I spectrum in the postprocessed temperature case has a continuum flux level below that of the optically thin, self-consistent case. Since the mean transmitted flux is sensitive to the number of pixels close to the continuum at low redshifts the line of sight average transmitted flux in the post processed calculation is below the value obtained from the self consistent calculation by about $\approx 8\%$. That was expected in our discussion in Section (3).

In the absorption spectra along the randomly casted sightlines there is an apparent lack of signatures marking the presence or not of the local ionizing sources. The spectra in the examples shown in Figure (7) look in general similar, although in some isolated regions the local amplitude clearly differs from a uniform UV background. This result is expected because at the time of reionization completion, the mean absorption in a random sightline spanning 2.4 times the length of the simulated cube is not sensitive to any local effects by the ionizing sources but rather depends on the value of the ionizing radiation at the level of the mean density and the density valleys.

We show on the left panels of Figure (8) a sightline with a path that takes the sightline about one mesh resolution element, ≈ 0.2 Mpc comoving, away from a UV source. On the top left panel, we show the Ly α He II transmission versus observed wavelength. Below, we plot the instantaneous comoving distance of each velocity pixel to the closest UV source versus the comoving path length of the sightline. The last curve is a joint ensemble of parabolic curves each having a minimum, marked with crosses, that corresponds to the position of nearest distance to the ionizing source. Each time another UV source becomes closest to the trajectory, the curve is marked by the beginning of another parabola. We note that at the location of closest proximity for that sightline, at ≈ 120 Mpc comoving along the path, the corresponding transmission is almost 1. Since the sources are placed at the high density dark matter peaks, which they subsequently follow during the dynamical evolution of the dark matter distribution, the absorption at that location is due to the UV source proximity. However, at a part of the spectrum about 1042 \AA , the high transmission there is due to a highly ionized underdense region since the closest point source is more than 20 Mpc comoving away. Therefore, from the information in the spectra alone, we will not be able to distinguish between transmission in a region close to an ionizing source or transmission from an underdense region.

We will call impact parameter each nearest distance to an ionizing source encountered by the sightline trajectory. On the right panel of Figure (8), we plot the sightline distribution of impact parameters in bins of constant size 1 Mpc. The upper horizontal axis converts comoving Mpc distances to proper separation velocities. The distribution is negatively skewed with a peak frequency (mode) located at ≈ 9 Mpc (≈ 550 km/s). Due to negative skewness, the mean is shifted to the right at a value of ≈ 14 Mpc (≈ 750 km/s). The negative skewness is most likely due to the fact that the distribution of the UV point sources on the grid is not isotropic but are clustered according to the clustering properties of the host dark matter halos. From the distribution in the right panel of Figure (8) we can compute a typical range of impact parameters in the sightlines of $\approx 2 - 22$ Mpc comoving contained within the values of the distribution at $1/e$ the peak value. We are interested to determine whether the transmission properties of our sightline sample is in any way biased by the proximity to the ionizing sources or if we are mostly sensitive to the values of the ionizing flux at the mean level.

Detailed analysis of the proximity effect around each source is beyond the scope of this paper. However, we can impose an upper bound limit based on the highest luminosity quasar in the computational volume at $z=2.5$, $L_4^{max} = 2 \times 10^{44}$ ergs/s where L_4 designates continuum ionizing luminosity above 4 Ryd. An estimate of a proximity size distance can be obtained from the

volume averaged energy density above the He II ionization threshold, \bar{E}_4 . In our calculation we have computed $\bar{E}_4 = 7.7 \times 10^{-17}$ ergs/cm⁻³ which corresponds to a volume averaged He II ionizing flux equal to $\bar{F}_4 = c\bar{E}_4 = 2.3 \times 10^{-6}$ ergs/s/cm⁻². The condition that the geometrical attenuation of the central emission equals the total flux through the surface of a sphere centered at the source yields an upper bound for this proximity distance of $d_{HeII}^{proper} \leq (L_4^{max}/4\pi\bar{F}_4)^{\frac{1}{2}} \simeq 0.86$ Mpc proper or $d_{HeII} \lesssim 3$ Mpc comoving. When compared to the comoving length of the sightlines (≈ 270 Mpc comoving) we expect that these regions do not have a large effect on the mean He II Ly α transmission value.

On the left panel of Figure (9), we show a quantitative estimate of that effect. There, we scatter plot the average impact parameter of the sightline versus the mean transmission in each sightline (cross symbols). The degree of their linear correlation, measured by the Pearson correlation coefficient, is rather small, $r = -0.24$. The figure does show that there is non-negligible negative correlation between mean transmission and the average proximity to the distribution of ionizing sources for each sightline. A power law fit to the data in the form $\bar{F}_{los} \propto \bar{d}_{ip}^{-s}$ where \bar{F}_{los} is the sightline specific mean flux and \bar{d}_{ip} is the average impact parameter yields $s = -0.16 \pm 0.04$ and is plotted over the individual points. The curve lies within the two standard deviations levels of the mean transmission. Therefore, we conclude that the proximity effects have no statistical weight on the sightline transmissions. That is consistent with our estimate of the upper limit on the proximity distance ($\simeq 3$ Mpc comoving) based on matching the attenuation of the point luminosity to the volume averaged ionizing flux. Since the typical range of the impact parameters is between 2-22 Mpc comoving our sightlines are on average too far away from the point sources. This conclusion is also supported by the right panel of Figure (9) where we show the scatter plot between the individual impact parameter values and the local He II Ly α absorbed flux at that distance from the point source (points). The data show a tail of low absorption at small impact parameters at distances $\lesssim 4.5$ Mpc comoving. The distribution of absorption above $\gtrsim 4.5$ Mpc is consistent with the mean level of absorption in the sightline sample, shown as a horizontal blue solid line along with upper and lower blue dashed lines corresponding to the 2σ level. To get a clear view of the trend we bin the horizontal axis into constant logarithmic bins and compute the median (red histogram) and mean (blue histogram) per bin. A Fermi-Dirac function in the form $f(x) = \frac{1}{1+\exp(\frac{do-x}{\mu})}$ is then fitted to the median histogram with $do = 3.1$ Mpc (point of half maximum) and $\mu = 0.63$ Mpc (skin width) for impact parameters up to 10 Mpc. The point of half maximum is consistent with the previous estimate of the proximity effect distance based on the luminosity and mean intensity of the UV field. The figure clearly shows that the effect of source proximity on the local absorbed flux are relevant at comoving distances of $\lesssim 7$ Mpc where the local absorption matches the mean He II Ly α absorption in the IGM and becomes significant at impact parameters $\lesssim 4.5$ Mpc comoving where the local absorption matches the lower 2σ level of the mean absorption.

6.2. Optical Depth Evolution

The straightforward average of the flux, $\bar{F} = \frac{1}{N_{px} \cdot n_{los}} \sum_j^{n_{los}} \sum_i^{N_{px}} F_{ij}$, from all pixels and lines of sight per redshift interval, is a measure of the opacity of the cosmic volume due to the absorption by the particular chemical species (He II and H I in this case). In the notation followed, $N_{px} = 30,000$ is the number of pixels per redshift interval, which yields a redshift pixel resolution of $R_z = \delta z = 0.2/30,000 \simeq 6.6 \times 10^{-6}$, and $n_{los} = 300$ is the number of random lines of sight. The redshift resolution is fixed in our calculation, which results in a redshift dependent spectral resolution of $R_\lambda = \frac{\lambda}{\Delta\lambda} = \frac{1+z}{\delta z} = 1.5 \times 10^5(1+z)$. At $z = 3$ this yields a spectral resolution of 50 times higher than the designed value of the spectrograph aboard FUSE.

The evolution of the mean transmitted flux is typically represented by the effective optical depth, defined as $\tau_{eff} = -\ln(\bar{F})$. As discussed in Paschos & Norman (2005) (PN), the effective optical depth is biased by high transmission gaps in the pixel flux distribution and therefore will systematically yield lower values when compared to the mean optical depth. The latter is defined as the raw average of the pixel optical depth per redshift interval, $\tau_{mean} = \frac{1}{N_{px} \cdot n_{los}} \sum_j^{n_{los}} \sum_i^{N_{px}} \tau_{ij}$, where τ_{ij} is the pixel optical depth at redshift z_i in the line of sight index $LOS = j$. In Figure (10), we show the redshift evolution of the the optical depth of the 304 Å line using both representations, mean (left panel) and effective (right panel), which suggests a rather smooth evolution leading to He II reionization at $z \simeq 2.5$. Error bars show the 1σ standard deviation of the mean flux and optical depth values between different lines of sight. In the effective optical depth case, standard deviation at more than 100% the mean flux value at $z \geq 5$ yield negative lower bound values. A cutoff in the mean flux of $F_{min} = 10^{-6}$ was therefore imposed in order to be able to compute the natural logarithm.

The error bars also indicate a large degree of variance in the data at redshifts $z \gtrsim 3.5 - 4$ consistent with PN which discussed properties of H I transmission during hydrogen reionization. There, the large degree of variance during reionization was attributed to the presence of high transmission gaps associated with underdense regions in the IGM which ionize first. In this picture of inhomogeneous He II reionization, the high transmission segments at high redshifts are associated with He III bubbles that the lines of sight intersect as they are cast through the simulation box. However, this is not inconsistent with the conclusions reached in PN because the He III bubbles primarily extend in underdense to mean density cosmic regions.

Estimates of the observed He II effective optical depth, shown in Figure (10), are comprised of the six known and analyzed sightlines to date: HS1700+6416 (Fechner et al. 2006; Davidsen et al. 1996), HE2347-4342 (Zheng et al. 2004b; Kriss et al. 2001), HS1157+3143 (Reimers et al. 2005), PKS1935-692 (Anderson et al. 1999), Q0302-003 (Heap et al. 2000) and SDSSJ2346-0016 (Zheng et al. 2004a). Although very few in number they suggest a lack of He II Ly α forest transmission at redshifts above $z \simeq 3$ and the presence of a trough there consistent with the hypothesis of late He II reionization. Upper bound estimates suggest a steeply rising optical depth above $z \simeq 2.8$ while lower bound estimates infer a smoother reionization transition. Lower redshift

sightlines towards HS1700+6416 (Fechner et al. 2006) and HE2347-4342 (Zheng et al. 2004b; Kriss et al. 2001) suggest an optical depth of about 1 between $z \simeq 2.3$ and $z \simeq 2.7$. In this work, we have calculated that between $z = 2.6 - 2.4$, at $\bar{z} = 2.5$, a mean transmitted flux value at $\bar{F} = 0.304 \pm 0.002$ which corresponds to $\tau^{eff} = 1.190 \pm 0.007$. The error to the mean values is due to sightline-to-sightline variance and is equal to $1\sigma/\sqrt{N_{los}}$. Observed effective optical depth estimates are $\tau_{obs}^{eff} = 0.91 \pm 0.01$ for HE2347-4342 averaged over $z \simeq 2.3 - 2.7$ and a range between $\tau_{obs}^{eff} = 0.74 \pm 0.34$ and $\tau_{obs}^{eff} = 1.06 \pm 0.18$ at $\bar{z} \simeq 2.45$ for HS1700+6416 (Fechner et al. 2006). If reionization is completed by $z \simeq 2.5$, as suggested by the observed lines of sight, that would correspond to an optical depth of $\tau_{eff} \simeq 1$. Our calculation is about 1.5σ above that value at that redshift. Furthermore, the computed redshift evolution of the optical depth is smoother than suggested by observations. We attribute such differences to the limitations of our treatment and most notably ignoring diffuse emission due to recombinations to the ground state of He II. Such recombinations increase the ionization of He II and therefore lower the opacity. The slope of the redshift evolution is affected by such omission because of the diffuse emission's dependency on the gas temperature, $\propto T^{-\frac{1}{2}}$. At earlier redshifts, the temperature is lower and therefore recombinations to the ground state may contribute a significant amount of He II ionizing radiation. Nonetheless, due to the lack of a self-consistent calculation we do not know how large that effect would be on the slope of the optical depth redshift evolution. We do anticipate that the effect diminishes with redshift due to photoheating which raises the IGM temperature.

From the right panel of Figure (10) we can infer a general agreement between the observed and computed values at redshifts that evidently sample the tail of the He II reionization epoch. That leads to the conclusion that the final opacity distribution in He II is largely insensitive to the details of our numerical setup. Direct photo-ionizations due to a rising number density of QSO sources appears to be adequate to yield a value of the He II abundance close to the observed one at late redshifts.

6.3. Line Statistics

The largely ionized He II by $z=2.5$ in our computational volume and the update in the gas temperature due to photo-heating, allows for the derivation of two standard statistical properties of a Ly α forest, the column density and b-parameter distribution. Our grid resolution is too coarse to draw any absolute conclusions about these distributions. In order to resolve the H I Ly α forest, a grid resolution of ~ 40 kpc is required (Bryan et al. 1999). A larger grid resolution may not be required for He II lines if they primarily form in underdense regions. However, comparison with a resolved H I forest is desirable. Our intent in this work is to look at the relative differences between the two forests and draw conclusions that may stand the test of an improved grid resolution in a future simulation.

Between $z=2.6-2.4$, at $\bar{z} = 2.5$, we identify the He II and H I Ly α lines and compute their column density and b-parameter width. The line identification was performed using the method

described in Zhang et al. (1998). We count lines per constant logarithmic column density bins ($\Delta N_X = 0.25$) and normalize per column density and redshift interval, $dz = 0.2$, for the two species, $\frac{d^2 N}{dz dN_X}$ ($X = \text{H I}, \text{He II}$). The result is shown in the left panel of Figure (11). The H I distribution flattens at $\text{Log} N_{\text{HI}} \sim 12.5$ which is due to the coarse grid resolution. A similar flattening occurs at $\text{Log} N_{\text{HeII}} \sim 13.5$. In addition, the He II column density distribution shows a decrease in the slope and large error bars as the column density increases. The error bars refer to the 1σ standard deviation of the identified line counts per logarithmic bin. By $\text{Log} N_{\text{HeII}} \gtrsim 17.5$ the dramatic increase in the error and hardening of the slope is interpreted as the effect of regions of He II that are not fully ionized by $z=2.5$. Such regions occupy about 10% of the computational volume and are a source of large optical depths and therefore column densities in lines of sight that pass through them. The two profiles suggest that for column densities in the range 13.5 - 15.5 we identify 10-100 times more He II than H I lines. This result is consistent with a high resolution cosmological simulation that resolves the two forests (Zhang et al. 1997).

Power law fits to the column density distributions in Figure (11), $f_X(N)dN_X = \beta N_X^{-\alpha_X} dN_X$, yield $\alpha_{\text{HI}} = 1.89 \pm 0.14$ and $\alpha_{\text{HeII}} = 1.41 \pm 0.12$ in the logarithmic column density range of 13.5 - 15.5. The error estimates are derived from the least squares fit and do not take into consideration any propagated error in the individual column density bins which is sensitive to the bin size. The Ly α forest is well studied in the literature, however results that are pertinent to the slope of the column density distribution typically refer to either the range of $\log N_{\text{HI}}(\text{cm}^{-2}) = 12.5 - 14.5$ or to an average slope between the minimum to maximum value in the column density sample. From distributions obtained in simulations (Zhang et al. 1997; Jena et al. 2005) and observations (Petitjean et al. 1993; Rauch et al. 1997; Kirkman et al. 1997) we have estimated a range in the slope of the distribution between $N_{\text{HI}} = 10^{13.5} - 10^{15.5} \text{ cm}^{-2}$ of $\alpha_{\text{HI}} = 1.7 - 1.85$ for redshifts between $z=2-3$. The slope for the H I column density distribution obtained in this work is slightly above. That is primarily due to the poor grid resolution that underestimates the number of H I absorbers with high column densities. To a lesser extent, we also expect a steepening in the distribution because we overestimate the H I opacity for lower column density absorbers in our numerical setup. However, we note that within the error estimate of the power law fit, the value of the slope we computed here overlaps with the range of published values.

The estimated slope of the He II Ly α column density distribution, in the optical thin limit, using uniform photoionization models, ranges between $\alpha_{\text{HeII}} \approx 1.5 - 1.6$ in the redshift interval $z=2-3$ and for $\log N_{\text{HeII}} = 13.5 - 15.5$ (Zhang et al. 1997). In this work, we have calculated the slope of the distribution at $\bar{z} = 2.5$ to be $\alpha_{\text{HeII}} = 1.41$ which is below the previous estimates. As we shall show below the He II absorbers correspond to physically extended IGM structures and therefore the He II column density distribution is less sensitive to our coarse grid resolution than hydrogen. The smaller slope is due to the opacity effects of the inhomogeneous ionizing radiation. Overdense regions will have higher opacity to He II ionizing radiation compared to a uniform photoionization model. That in turn results in lines migrating to higher column density bins which softens the slope of the distribution compared to an optically thin calculation.

We now proceed to investigate the effects of non-uniform photoheating in the distribution of the line broadening widths which is the observable that closely traces the thermal state of the IGM. The b-parameter distribution, computed here as the fraction of lines per km/s is shown for the two species on the right panel of Figure (11) (solid lines). The distributions were computed from lines with column densities in the range $\text{Log}N_X = 13.5 - 15.5$ for both species. The selected range aims to avoid the undersampling of weak lines due to the coarse grid resolution. For reference, we also plot the b-parameter distribution computed from a uniform photoionization optically thin simulation due to a Haardt & Madau (2001) UVB model from a mix of quasar and galaxy populations (dashed lines). The median line broadening widths derived in the non-uniform UV case are $b_{med}^{HI} = 34.23 \text{ km s}^{-1}$ and $b_{med}^{HeII} = 28.16 \text{ km s}^{-1}$ for the H I and He II lines respectively. For comparison, the median values in the uniform UVB case are $b_{med}^{HI}(u) = 32.98 \text{ km s}^{-1}$ and $b_{med}^{HeII}(u) = 26.89 \text{ km s}^{-1}$. When we compare the non-uniform and uniform results we note that the peaks of the distributions are offset by $\simeq 1.25 \text{ km/s}$ in both species. This is expected according to the right panel of Figure (5) where the median temperature per logarithmic overdensity bin is plotted. Differences in the overdensity dependent median temperature distribution arise at overdensities $\Delta \lesssim 3$. If we adopt a relation between H I column density and overdensity in the form of $\Delta \geq 10(\frac{N_{HI}}{10^{15}})^{2/3}(\frac{1+z}{4})^{-3}$ (Schaye et al. 2003) then we can compute that at $z=2.5$ a H I column density of $10^{13.5} \text{ cm}^{-2}$ is due to overdensities of $\Delta \gtrsim 1.5$. At such overdensities we predict the biggest difference in the temperature between the non-uniform versus the uniform cases. The increase in temperature by a factor $\simeq 1.6$ is consistent with a shift in the peak of the b-parameter distribution. Note however, that the distributions at broadening widths larger than 50 km/s are indistinguishable which may be due to collisional ionization dominating the line opacity.

Since the forests are unresolved on the simulation grid, we make no claim on whether the computed b-parameter values have any relevance to the real universe. We can however compare the median values of the two species. Relative to hydrogen the median values infer that on average the He II lines have about $\approx 82\%$ the broadening width of the H I lines. For pure thermal broadening, the heavier by a factor of 4 helium atoms would yield a width only half the corresponding size of the hydrogen line, $b_{th}^{HeII} = \frac{1}{2}b_{th}^{HI}$. Our calculation suggests that the broadening due to the Hubble differential flow and peculiar velocities dominate the line formation in the He II forest. That in turn would indicate that the He II lines primarily form in underdense and cosmic mean density regions. Our result is consistent with the conclusions in Zheng et al. (2004) where they calculated that along the HE2347-4342 transmission line $b_{HeII} \simeq 0.95b_{HI}$ which also supports a Hubble dominated absorption line broadening for He II.

6.4. η -Parameter Evolution

We conclude this section, by computing the redshift evolution of the η -parameter through the R-factor, which are defined in §2.2. In Figure (12), we plot the redshift evolution of the η -parameter in the range $3.5 \leq z \leq 2.5$ in redshift intervals of $\delta z = 0.2$, averaged over all lines of

sight. Direct computation of the quantity not only requires knowledge of the column density for each individual line but also knowledge of the local association between the H I and He II absorption features. However, because the transmission of the He II Ly α line exhibits a trough at redshifts $z \gtrsim 3$, obtaining the column density value for individual He II lines is not feasible there due to the inability to deblend the absorption features in the spectrum. In addition, whatever correlation between the H I and He II lines exists at $z \lesssim 3$ it would be incomplete because not all H I lines can be associated with He II absorption features and vice versa (Kriss et al. 2001). Our biggest problem though in this calculation lies in the separate treatment of hydrogen and helium ionization. The latter coupled to a low resolution simulation can be a source of significant bias against the true correlation between the He II and H I absorbers.

Therefore, we will approximate here the line of sight and redshift interval average of the η -parameter as $\langle \log(\eta) \rangle \simeq \langle \log(4 \times \frac{\tau_{\text{HeII}}}{\tau_{\text{HI}}}) \rangle = \langle \log(4 \times R) \rangle$ where R stands for the R-factor. Through this approximation, the identification of individual lines and the derivation of column density through their gaussian profiles are not required. Instead, in each redshift interval we compute the average of the ratio between the local He II and H I pixel optical depths along the transmission line. The values for each line of sight are then averaged to obtain a mean value for the η -parameter. We plot the redshift evolution of such calculation in Figure (12). Because the errors due to pixel averaging are large, they are ignored. Instead, the error bars in the figure represent the 1σ standard deviation due to line of sight averaging. For reference, we overplot the computed value of the η -parameter in the spectrum of HE2347-4342 from Kriss et al. (2001) and also data from Fechner et al. (2006) (blue circle) towards HS1700+6416. We obtained the latter by computing the mean $\log\eta$ from the published data in the range $z=2.3-2.75$. At $z=2.5$ our computed value $\log\eta = 2.1 \pm 0.1$ is above the observed values which is mainly due to our larger estimate of the He II Ly α optical depth at that redshift. As with the optical depth calculation, the limitations of our treatment result in an overestimate. However, we came close enough to the observed values at redshifts later than the He II transmission trough, to reinforce our conclusion that our limited calculation is able to reproduce the much of the observed signatures of He II reionization.

7. Summary & Conclusions

We have simulated the late inhomogeneous reionization of He II by quasars and the attendant photoheating of the IGM including opacity effects. We post-process baryonic density fields from a standard optically thin IGM simulation with a homogeneous galaxy-dominated UV background which reionizes H I and He I at $z=6.5$. Quasars are introduced as point sources throughout the 100 Mpc simulation volume located at density peaks consistent with the Pei luminosity function. We assume an intrinsic quasar spectrum $J(\nu) \propto \nu^{-1.8}$ and a luminosity proportional to the halo mass. We evolve the spatial distribution of the He II ionizing radiation field at $h\nu = 4, 8$, and 16 Ryd using a time-implicit variable tensor Eddington factor radiative transfer scheme which we describe. Simultaneously, we also solve for the local ionization of He II to He III and the associated

photoheating of the gas. This distinguishes our calculation from the work of Sokasian, Abel and Hernquist (2002) who simulated inhomogeneous He II reionization but did not study the thermal evolution of the gas.

We find that the cosmic evolution of the QSO population causes the individual He III regions to overlap and subsequently ionize 90 % of the volume at He III ionization fractions $\psi_3 = \frac{n_{\text{He III}}}{n_{\text{He}}} \gtrsim 10^{-5}$ by $z \simeq 2.5$. In addition, to the He II and He III number density calculation, we also update the local gas temperature due to the thermalization of the photoelectrons ejected by the He II ionization process. As expected, the temperature is higher compared to the unprocessed simulation with the difference increasing rapidly at redshifts $z \lesssim 3$. Relative to a self-consistent optically thin simulation where He II is also photoionized by a homogeneous UV background, we find that optical depth effects result in an increase in the temperature of the intergalactic medium at the cosmic mean density level by a factor of ≈ 1.7 at $z = 2.5$. The results of our temperature calculation are consistent with analytic and numerical predictions of the He II heating effect (Abel & Haehnelt 1999; Schaye et al. 2000; McDonald et al. 2000). Finally, we trace the redshift evolution of the He II Ly α transmission using randomly casted synthetic spectra through the simulated volume. The analysis of the mean transmission allows for the derivation of the effective optical depth of the 304 Å line.

We have calculated that at $\bar{z} = 2.5 \pm 0.1$, the average of pixel flux among all lines of sight yields a value for the mean transmission of $\bar{F} = 0.304 \pm 0.002$ which corresponds to $\tau_{304}^{eff} = 1.190 \pm 0.007$. The length of each sightline ($\Delta z = 0.2$) is longer than the size of the simulation in order to minimize the transmission variance across the redshift path. We compute the error only due to the sightline to sightline variance and find that at $z=2.5$ the 1σ standard deviation is 11% the mean Ly α flux. When we compare to estimates from He II forest spectra observed with the FUSE (Far Ultraviolet Space Explorer) satellite and HST at the same redshift interval we find that the our value of the effective depth is comparable but slightly above the observed values. We attribute the disagreement to our approximate treatment of the inhomogeneous ionizing radiation that ignores the diffuse component and only focuses on the point sources’ input.

In addition to the mean transmission estimate, we also compute the column density and b-parameter distribution of the identified He II Ly α lines and compare them to the corresponding statistical properties of the H I Ly α lines. We find that an optically thick calculation results in extra heating that shifts the b-parameter distributions to higher broadening widths. In addition and within the limitations of our coarse numerical resolution, which does not resolve the H I forest, our calculation shows that the median He II b-parameter at $\bar{z} = 2.5$ is 82% the H I broadening width. The latter suggests that the Hubble differential flow may be the dominant line broadening mechanism which in turn indicates that He II lines primarily form in underdense to cosmic mean density regions.

ACKNOWLEDGEMENTS

This work was supported by NSF grants AST-9803137, AST-0307690 and AST-0507717. The simulations were carried out on the TITAN IA64 Linux cluster at the National Center for Super-

computing Applications and on the IBM Blue Horizon system at San Diego Supercomputing Center under LRAC allocation MCA098020.

A. Species Concentration Equation in an Expanding Universe

For a single species medium and in proper coordinates the rate equation that governs the abundance of ionization state i is given by the following equation:

$$\dot{n}_i = -3\frac{\dot{a}}{a}n_i + \Sigma_j \beta_{ij}n_j \quad (\text{A1})$$

In Equation (A1), n_j denotes the number density of ionization states of the species in ionization or recombination coupling to state i . The ratio $\frac{\dot{a}}{a}$ is a function of redshift and is equal to the redshift value of the Hubble constant.

Dividing by the total number density of the species, n_T , we get:

$$\begin{aligned} \dot{n}_i/n_T &= -3\frac{\dot{a}}{a}n_i/n_T + \Sigma_j \beta_{ij}n_j/n_T \Rightarrow \\ \dot{n}_i/n_T &= -3\frac{\dot{a}}{a}y_i + \Sigma_j \beta_{ij}y_j \end{aligned} \quad (\text{A2})$$

The LHS of Equation (A2), can be rewritten as follows:

$$\begin{aligned} \frac{1}{n_T} \frac{\partial}{\partial t} n_i &= \frac{\partial}{\partial t} \left(\frac{n_i}{n_T} \right) - n_i \cdot \frac{\partial}{\partial t} \left(\frac{1}{n_T} \right) = \\ &= \frac{\partial}{\partial t} y_i + \frac{1}{n_T^2} \dot{n}_T n_i = \dot{y}_i - 3\frac{\dot{a}}{a}y_i \end{aligned} \quad (\text{A3})$$

Plugging the result back into Equation (A2), we get $\dot{y}_i = \Sigma_j \beta_{ij}y_j$, which shows that when solving the rate equation using ionization fractions, instead of number densities, the equation is independent of the Hubble expansion term. However, coefficients β_{ij} that are pertinent to recombinations to state i depend on the electron density which is computed on the proper frame of reference.

B. Effect of Late Reheating on Hydrogen Ionization Balance

In this calculation, we estimate the neutral hydrogen fraction if an additional source of ionization and heating is introduced due to the full photoionization of He II by a local UV radiation

followed and the ejection of an additional electron per helium atom, assumed to be already singly ionized. The unmodified neutral fraction is labeled as Case (I). Case (II) represents the updated hydrogen abundance.

In Figure (13), Equation (6) was solved for two values of temperature increase, $T^{II}/T^I = 1.5 - 2$. On the left panel we show the neutral hydrogen fractions in Case (II) for a range of Case (I) inputs. The open squares (circles) represent the smallest (largest) temperature increase. The solid line stands for no difference between the two cases (slope of 1). The calculation shows that the largest temperature increase results in a greater departure from the straight line, although the degree of such departure becomes smaller at larger neutral fractions.

This is shown on the right panel of Figure (13) where we plot the percentage change in the hydrogen neutral fraction. We see a fixed degree of change between $\chi_1^I = 10^{-6} - 10^{-2.5}$ and a rapid decrease at $\chi_1^I \gtrsim 10^{-2.5}$. For the range of temperature increase used in the calculation we can then determine that a total He II photoionization would lead to an adjustment of the hydrogen neutral fraction by 12-24%. This corresponds to an overestimate of χ_1 , in the absence of He II photoheating, by $\approx 14 - 32\%$.

The degree at which any temperature change affects the hydrogen ionization balance is sensitive to the functional form of the recombination coefficient. In general, the coefficient steepens at temperatures above $T \simeq 10^4$ K where the slope becomes a function of temperature itself. The results shown in Figure (13) are derived with a constant slope of $\beta = 0.5$ which is roughly valid at $T \simeq 10^4$ K. To explore the effects of the slope on the adjustment of the hydrogen neutral fraction, due to He II photoheating, we show on the left panel of Figure (14), the results of the calculation for an input neutral fraction of $\chi_1^I = 10^{-5}$, $\beta = (0.4, 0.5, 0.6)$ and for a range of temperature ratios (0.5-2.0).

The upper dashed line at $T^{II}/T^I \geq 1$ represents the largest β value (0.6) and indicates that a steepening of the temperature exponent leads to an increase in the neutral hydrogen fraction adjustment. This trend is reversed at $T^{II}/T^I < 1$ (cooling). The latter temperature adjustment range is not related to any He II photoheating effects but it was a numerical investigation of the solution. However, one can make the argument, depending on whether the UVB drops after a certain redshift, that additional cooling terms, such as collisional ionization cooling ($He_{II} + e^- \rightarrow He_{III} + 2e^-$) and recombination radiation cooling ($He_{III} + e^- \rightarrow He_{II} + \gamma$), might lower the temperature below the unperturbed value. However, such possibility is small at least up to $z \simeq 2$.

We also note from the left panel of Figure (14) that not all values of a temperature increase lead to a positive neutral hydrogen fraction adjustment ($1 - \frac{\chi_1^{II}}{\chi_1^I} \geq 0$). In the $\beta = 0.5$ case (solid curve) a small increase of the temperature by less than 15% adjusted to a larger value and therefore $1 - \frac{\chi_1^{II}}{\chi_1^I} \leq 0$. This is a result of the increased electron number density due to the additional photoelectron ejected from the He II atom. In this narrow range of temperature increase the greater electron number density dominates the recombination rate, which consequently increases to shift the ionization balance towards more neutral hydrogen.

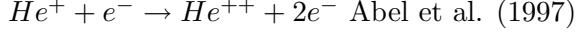
This effect depends on the initial neutral fraction, as shown on the right panel of Figure (14). There, we plot the family of solutions of Equation (6) ($\beta = 0.5$) for the range of neutral fractions ($10^{-6} \leq \chi_1^I \leq 10^{-1}$) and temperature adjustment factors ($0.5 \leq T^{II}/T^I \leq 2.0$). The solid line represents the solution obtained for $\chi_1^I = 10^{-5}$ from the left panel. The plot shows that as the neutral fraction increases the adjustment decreases for $T^{II}/T^I \geq 1$. As discussed in the previous paragraph, the range of T^{II}/T^I where the electron density dominates the recombination rate shifts to the right towards lower ionization fractions.

C. Radiative and Collisional Rates

In this section we document the radiative and collisional rates we used in our simulation. For the full range of chemical reaction rates incorporated into the cosmological hydro code Enzo please see Anninos et al. (1997) and Abel et al. (1997).

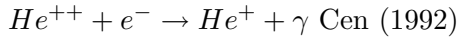
C.1. Collisional Ionization and Radiative Recombination of Singly Ionized Helium

Fits are accurate within 1% in the temperature range $1 - 10^8$ K.



In the following fit temperature T is in units of eV: $T = \frac{T}{11600 \text{ K}}$

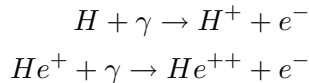
$$\begin{aligned} \Gamma_2^{ion}/n_e \equiv k_5 = & \exp[-68.71050990 + 43.93347633 \ln(T) \\ & - 18.4806699 \ln(T)^2 + 4.70162649 \ln(T)^3 - 0.76924663 \ln(T)^4 + \\ & 8.11042 \times 10^{-2} \ln(T)^5 - 5.32402063 \times 10^{-3} \ln(T)^6 + \\ & 1.97570531 \times 10^{-4} \ln(T)^7 - 3.16558106 \times 10^{-8} \ln(T)^8] \text{ cm}^3 \text{ s}^{-1} \end{aligned}$$



$$\alpha_R^2 \equiv k_6 = 3.36 \times 10^{-10} T^{-1/2} \left(\frac{T}{1000 \text{ K}} \right)^{-0.2} \left(1 + \left(\frac{T}{10^6 \text{ K}} \right)^{0.7} \right)^{-1} \text{ cm}^3 \text{ s}^{-1}$$

Temperature is expressed in K.

C.2. Photoionization cross section of Hydrogen and Helium II



The cross section for both rates are expressed through the same functional form because singly ionized helium is a hydrogen like atom (from Osterbrock 1974).

$$\sigma = \frac{A}{Z^2} \left(\frac{\nu}{\nu_Z} \right)^4 \frac{\exp[4-4(\arctan \epsilon)/\epsilon]}{1-\exp(-2\pi/\epsilon)}$$

$$A = 6.30 \times 10^{-18} \text{ cm}^2, \epsilon = \left(\frac{\nu}{\nu_Z} - 1 \right)^{1/2} \text{ and } \nu_Z = 13.6 \times Z^2 \text{ (} Z = 1, 2 \text{)}.$$

For consistency with the notation used in the main text, we need to clarify that we label $\nu_1 \equiv \nu_{(Z=1)}$, $\nu_2 \equiv \nu_{(Z=2)}^{HeI}$ and $\nu_3 \equiv \nu_{(Z=2)}^{HeII}$.

For numerical convenience we use an approximation to the full He II cross section in the form $\sigma_{HeII} = \frac{A}{4} (= \sigma_{HeII}^o) \left(\frac{h\nu}{h\nu_3} \right)^{-3}$, where $h\nu_3 \equiv 54.4 \text{ eV}$. Such an expression allows an analytic calculation and fast reconstruction, via a polynomial fit, of the energy density profile between four frequency points. The power law approximation of the cross section is estimated to be accurate to within $\approx 3\%$ (Haehnelt & Abel 1999).

REFERENCES

- Abel, T., & Haehnelt, M. 1999, *ApJ*, 520L, 13
- Aguirre, A., Schaye, J. & Theus, T. 2002, *ApJ*, 576, 1
- Anderson, S. F., Hogan, C. J., Williams, B. F. & Carswell, R. F. 1999, *AJ*, 117, 56
- Anninos, P., Zhang, Y., Abel, T. & Norman, M. L. 1997, *NewA*, 2, 209
- Bertschinger, E. & Gelb, J. M. 1991, *ComPh*, 5, 164
- Bolton, J., Meiksin, A. & White, M. 2004, *MNRAS*, 348L, 43
- Bryan, G. L. & Norman, M. L. 1997, in *IMA workshop in Mathematics and Applications*, Vol. 117, p. 165 (Kluwer Academic)
- Bryan, G. L., Machacek, M., Anninos, P. & Norman, M. L. 1999, *ApJ*, 517, 13
- Bryan, G. L. & Machacek, M. E. 2000, *ApJ*, 534, 57
- Carswell, R. F., Webb, J. K., Baldwin, J. A. & Atwood, B. 1987, *ApJ*, 319, 709
- Carswell, R. F. 1989, *Nature*, 341, 692
- Cen, R. 1992, *ApJS*, 78, 341
- Cen, R., Miralda-Escudé, J., Ostriker, J. P., & Rauch, M. 1994, *ApJ*, 437, L9
- Ciardi, B., Ferrara, A. & White, S. D. M. 2003, *MNRAS*, 344, 7
- Davé, R., Hernquist, L., Weinberg, D. H. & Katz, N. 1997, *ApJ*, 477, 21

- Davidson, A. F., Kriss, G. A. & Zheng, W. 1996 , Nature, 380, 47
- Efstathiou, G. 1992, MNRAS, 256P, 43
- Eisenstein, D. & Hut 1998, ApJ, 498, 137
- Eisenstein, D. & Hu, W. 1999, ApJ, 511, 5
- Fechner, C., Reimers, D., Kriss, G. A. et al. 2006, A&A, 455, 91
- Giroux, M. L. & Shapiro, P. R. 1996, ApJS, 102, 191
- Gnedin, N. Y., & Abel, T. 2001, NewA, 6, 437
- Haardt, F. & Madau, P. 1996, ApJ, 461, 20
- Haardt, F. & Madau, P. 2001, in XXI Moriond Astrophysics Meeting, Galaxy Clusters and the High Redshift Universe
- Haehnelt, M. G., & Steinmetz, M. 1998, MNRAS, 298, 21
- Heap, S. R. et al. 2000, ApJ, 534, 69
- Hernquist, L., Katz, N., Weinberg, D. H. & Miralda-Escudé, J. 1996, ApJ, 457L, 51
- Hu, E. M., Cowie, L. L., McMahon, R. G., et al. 2002, ApJ, 568, L75
- Hui, L. & Gnedin, N. Y. 1997, MNRAS, 292, 27
- Jacobsen, P., et al. 1994, Nature, 370, 35
- Jacobsen, P., Jansen, R. A., Wagner, S. & Reimers, D. 2003, A&A, 397, 891
- Jena, T., Norman, M., L., Tytler, D., Kirkman D., et al. 2005, MNRAS, 361, 70
- Katz, N., Weinberg, D. H. & Hernquist, L. 1996, ApJS, 105, 19
- Kirkman, D. & Tytler, D. 1997, ApJ, 484, 672
- Kriss, G. A., et al. 2001, Science, 293, 1112
- McDonald, P., Miralda-Escudé, J., Rauch, M., Sargent, W. L. W. et al. 2000, ApJ, 543, 1
- Mihalas, D. & Mihalas, B. W., 1984, "Foundation of Radiation Hydro dynamics", Oxford University Press, New York
- Miralda-Escudé & Ostriker 1990
- Miralda-Escudé, J. & Rees, M. J. 1994, 266, 343

- Miralda-Escudé, J., Cen, R., Ostriker, J. P. & Rauch, M. 1996, ApJ, 471, 582
- Norman, M. L., Paschos, P., & Abel, T. 1998, H_2 in the Early Universe, ed. F.Palla, E. Corbelli, & D. Galli (Mem. Soc. Astron. Italiana), 69, 271
- Osterbrock, D. E., 1989, “Astrophysics of Gaseous Nebulae and Active Galactic Nuclei”, University Science Books, Mill Valley, CA
- Paschos, P., Norman, M. L., 2005, ApJ, 631, 59
- Pei, Y. C. 1995, ApJ, 438, 623
- Petitjean, P., Webb, J. K., Rauch, M., Carswell, R. F. & Lanzetta, K. 1993, MNRAS, 262, 499
- Rauch, M., Miralda-Escudé, J., Sargent, W. L. W., Barlow, T. A., Weinberg, D. H., Hernquist, L., Katz, N., Cen, R. & Ostriker, J., P., 1997, ApJ, 489, 7
- Razoumov, A., Norman, M. L., Abel, T. & Scott, D. 2002, ApJ, 572, 695
- Reimers, D., Koller, S., Wisotski, L., Groote, D., Rodriguez-Pascual, P. & Wamsteker, W. 1997, A & A, 327, 890
- Reimers, D., Fechner, C., Hagen, H.-J. et al. 2005, A&A, 442, 63
- Schaye, J., Theuns, T., Leonard, A. & Efstathiou, G. 1999, MNRAS, 310, 57
- Schaye, J., Theuns, T., Rauch, M., Efstathiou, G. & Sargent, W. L. W. 2000, MNRAS, 318, 817
- Sokasian, A., Abel, T. & Hernquist, L. 2002, MNRAS, 332, 601
- Theuns, T., Leonard, A. & Efstathiou, G. 1998, MNRAS, 297L, 49T
- Theuns, T., Schaye, J. & Haehnelt, M., G. 2000, MNRAS, 315, 600T
- Tytler, D., Kirkman, D., O’Meara, J. M., Suzuki, N., Orin, A., Lubin, D., Paschos, P., Jena, T., Lin, W., Norman, M. L. & Meiksin, A., 2004, ApJ, 617, 1
- Wadsley, J. W. & Bond, J. R. 1997, ASPC, 123, 332W
- Whalen, D., Abel, T. & Norman, M. L. 2004, ApJ, 610, 14W
- Zaldarriaga, M., Seljak, U. & Hui, L. 2001, ApJ, 551, 48Z
- Zaldarriaga, M., Hui, L. & Tegmark, M. 2001, ApJ, 557, 519Z
- Zhang, Y., Anninos, P. & Norman, M. L. 1995, ApJ, 453L, 57Z
- Zhang, Y., Anninos, P., Norman, M. L. & Meiksin, A. 1997, ApJ, 485, 496
- Zhang, Y., Meiksin, A., Anninos, P. & Norman, M. L. 1998, ApJ, 495, 63Z

Zheng, W., Chiu, K., Anderson, S. F., et al. 2004a, AJ, 127, 656

Zheng, W., Kriss, G. et al. 2004, ApJ, 605, 631Z

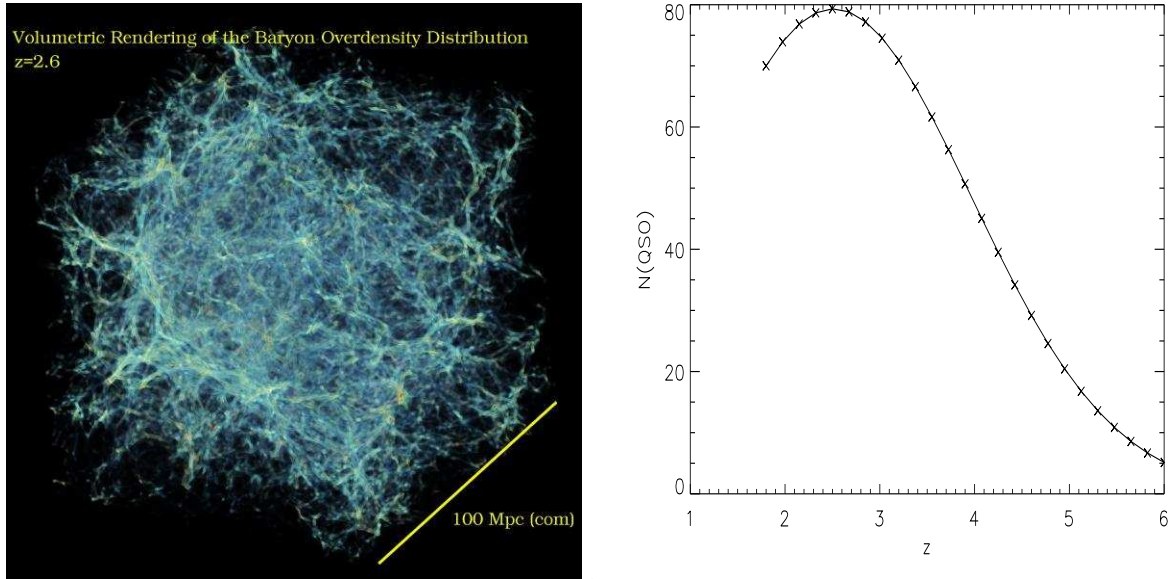


Fig. 1.— Left Panel: Volumetric rendering of the logarithm of baryon overdensity at $z=2.6$. Right Panel: Evolution in the number of QSO sources versus redshift in this simulation

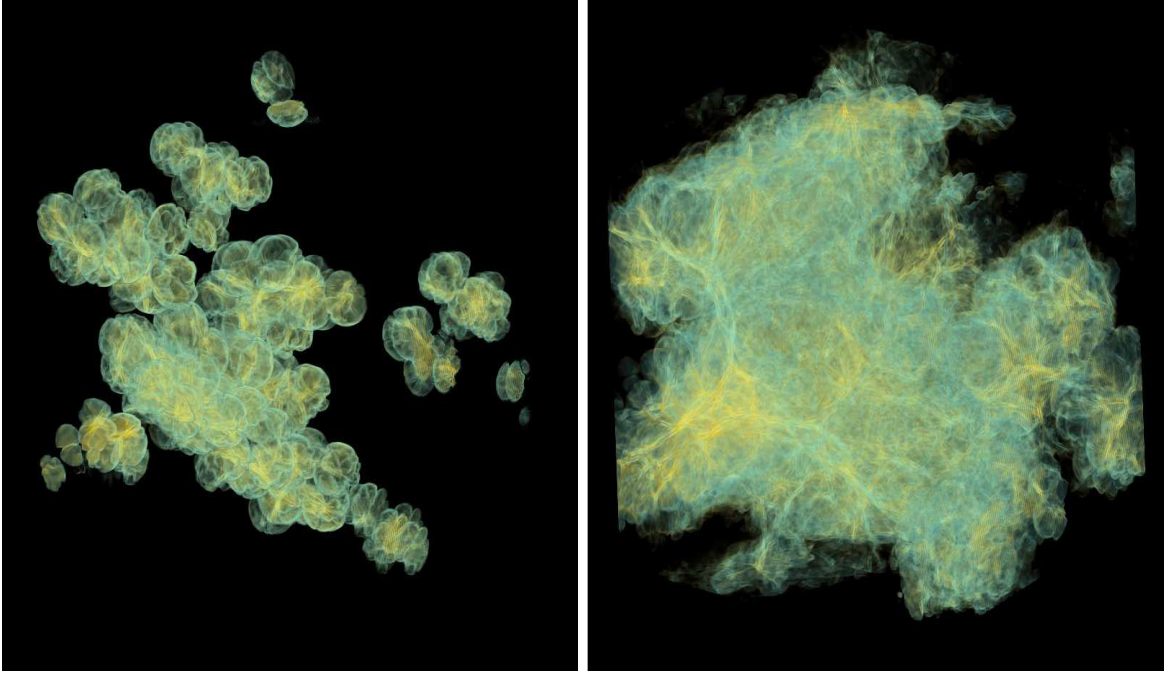


Fig. 2.— Volumetric renderings of the He III distribution mapped by the $\text{Log} n_{\text{He III}}$ at $z=3$ and $z=2.6$. The ionization cutoff in this visualization is set to $\psi_3 \equiv \frac{n_{\text{He III}}}{n_{\text{He}}} = 10^{-5}$ (dark regions).

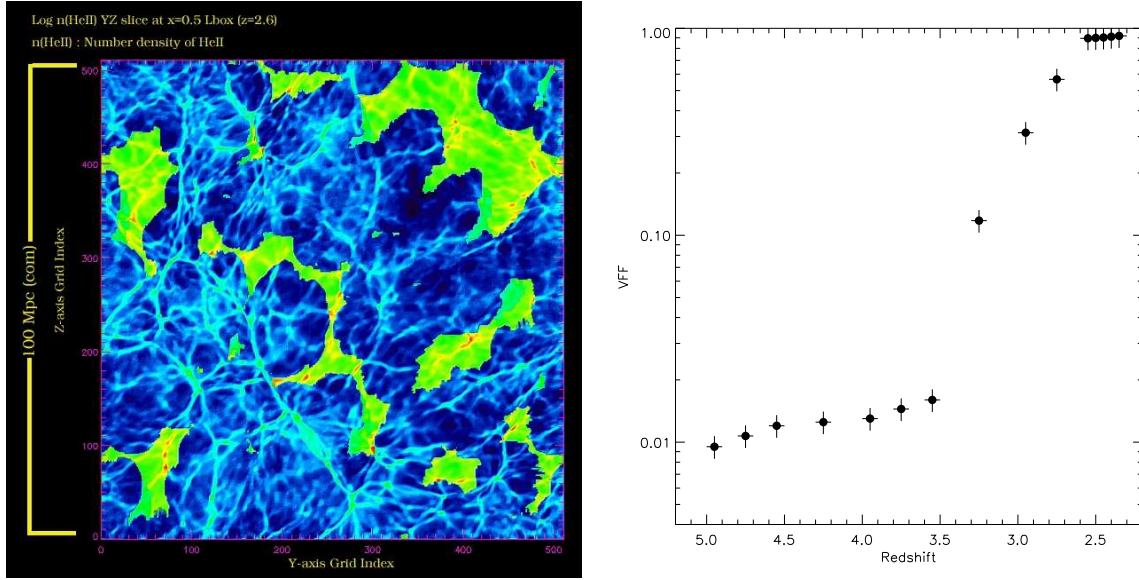


Fig. 3.— Left Panel: Slice of the He III (darkened regions) and He II 3D mass distribution at $z=2.6$. At that redshift, the volume filling fraction of the He III is $VFF \simeq 0.90$. Right Panel: Redshift Evolution of the VFF for $\chi_{HeIII} \geq 10^{-5}$. The error bars result from the uncertainty in the location of the cumulative I-front due to finite grid cell size.

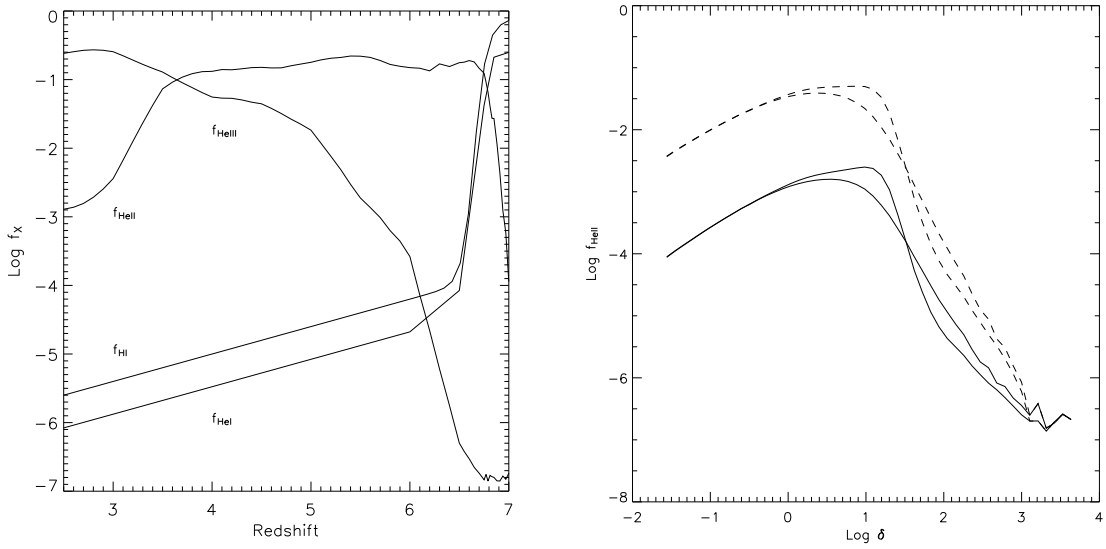


Fig. 4.— Left Panel: Redshift evolution of the volume averaged mass fraction of singly helium. Overplotted is the corresponding neutral hydrogen mass fraction. Right Panel: The scatter plot between HeII fraction and local gas overdensity at $z=2.5$ yields the mean and median value of $\text{Log } f_{\text{HeII}}$ per logarithmic bin of gas overdensity. Solid (dashed) curves refer to the inhomogeneous (homogeneous) case. The median profiles correspond to the curves that peak at $\text{Log } \delta \simeq 1$ in each case (the mean profiles peak at a lower overdensity).

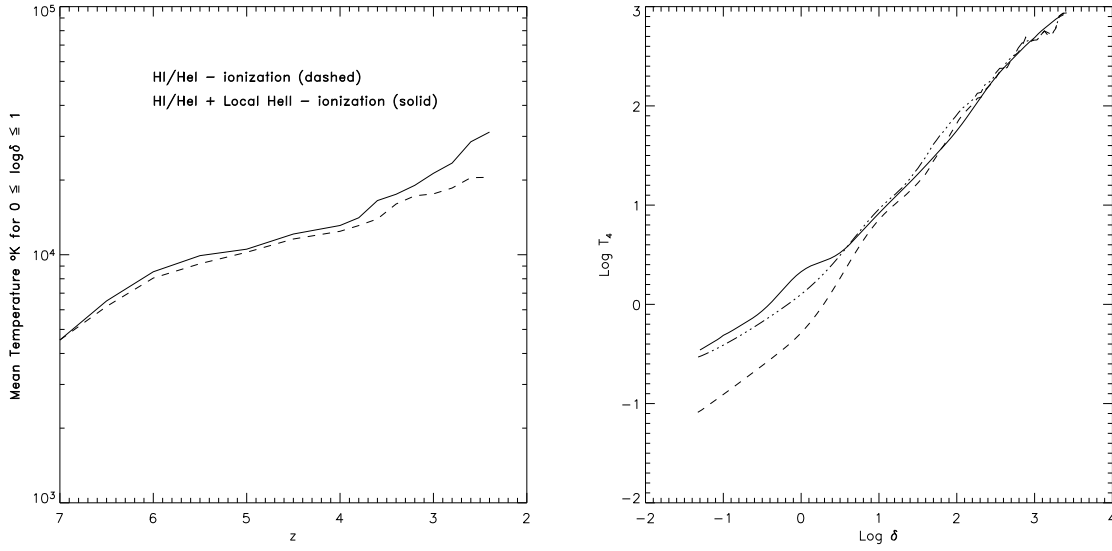


Fig. 5.— Left Panel: Redshift of the temperature evolution. Shown as a solid (dashed) line is the evolution in the processed (pure) case of the mean temperature in grid cells with overdensities between $\delta = 1 - 10$. Right Panel: The median temperature distribution in each logarithmic overdensity interval at $z=2.5$. It shows that the processed (solid) and unprocessed (dashed) cases. The curves show that He II reionization primarily increases the temperature of the IGM in low to mildly overdense range.

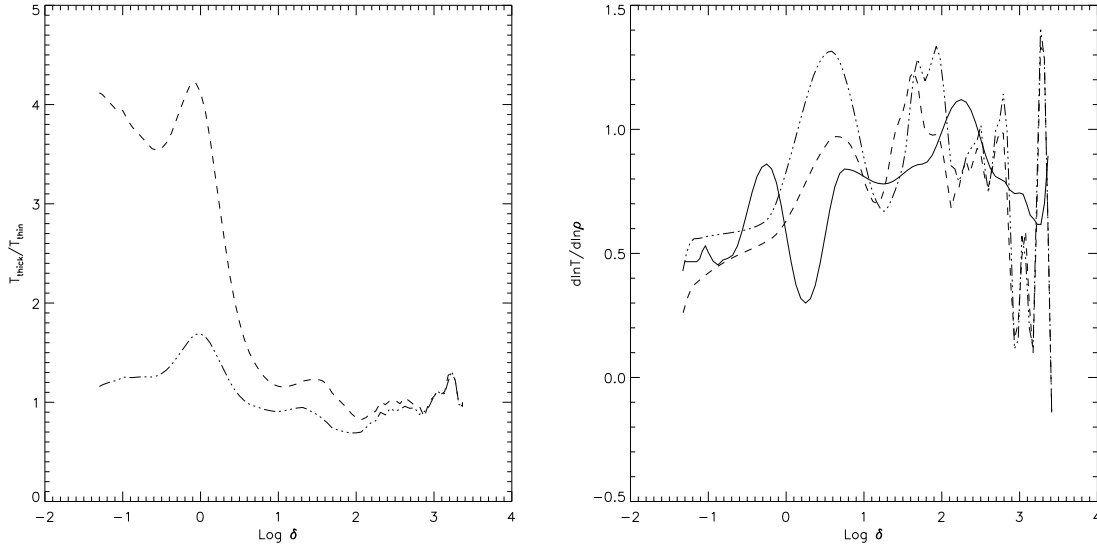


Fig. 6.— Left Panel: From temperature-density plot in Figure (5) we compute the ratio of the postprocessed result over the input simulation (dashed) and the optically thin simulation (dashed-dot). Right Panel: We plot the distribution of the logarithmic slope $\frac{d \ln T}{d \ln \rho} = \gamma - 1$ versus the gas overdensity density.

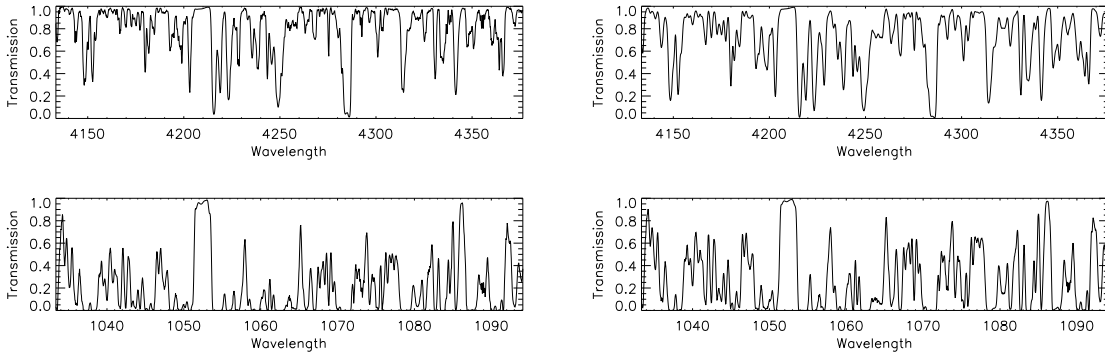


Fig. 7.— He II and H I Ly α spectra between $z = 2.6 - 2.4$, at $\bar{z} = 2.5$, along a randomly casted sightline through the computational volume. The upper panels refer to the H I Ly α transmission. The lower panels refer to the He II Ly α transmission. The horizontal axis is converted to observed wavelength $\lambda = \lambda_o(1 + z)$, where λ_o is the restframe wavelength of the resonant Ly α scatter. Left Panels: Uniform UVB ionizes and heats the IGM in the optically thin approximation. He II ionization and heating is included in this calculation. Right Panels: The uniform UVB only ionizes H I to H II and He I to He II. Photoheating therefore due to the uniform UVB only refers to the above processes. The non-uniform point source radiative input from QSO type sources is used to photoionize He II to He III and to calculate the subsequent photoheating. Although the H I spectra seem similar between the two sets of calculations, ignoring the feedback on H I abundance by the He II ionization results in underestimating the mean H I Ly α transmission, compared to the full simulation, by $\approx 8\%$.

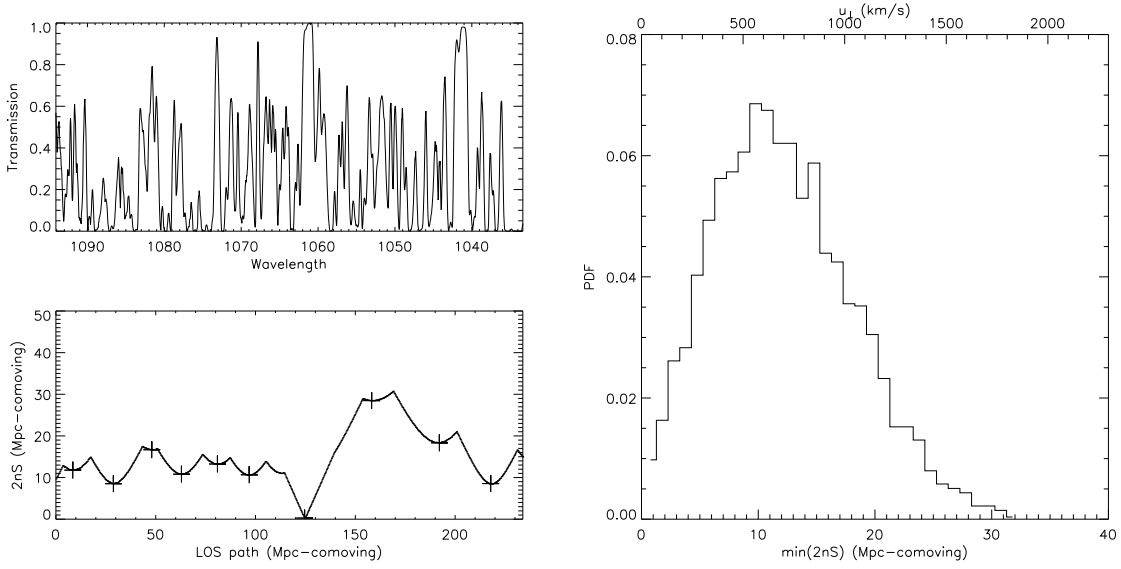


Fig. 8.— Impact parameters of the random sightlines to the point sources in the box at $\bar{z} = 2.5$. At each point along the path of the sightline, we compute the distance to the closest point source. As the trajectory crosses the computational volume, the closest source changes depending on position. On the lower left part of the figure, we plot this proximity distance for a sightline that comes the closest to a point source, about one grid resolution element. On the top left panel, we show the He II transmitted flux for that sightline. Crosses mark the locations along the path that are closest to the point source. The alternating proximity sources are indicated by the alternating parabolic profiles. On the right panel, we show the probability distribution of the minimum distance to the sources, which we define as the impact parameter, from all random sightlines. The asymmetry in the distribution is small, which is due to the near isotropic distribution of high density peaks at the scale of the simulated volume.

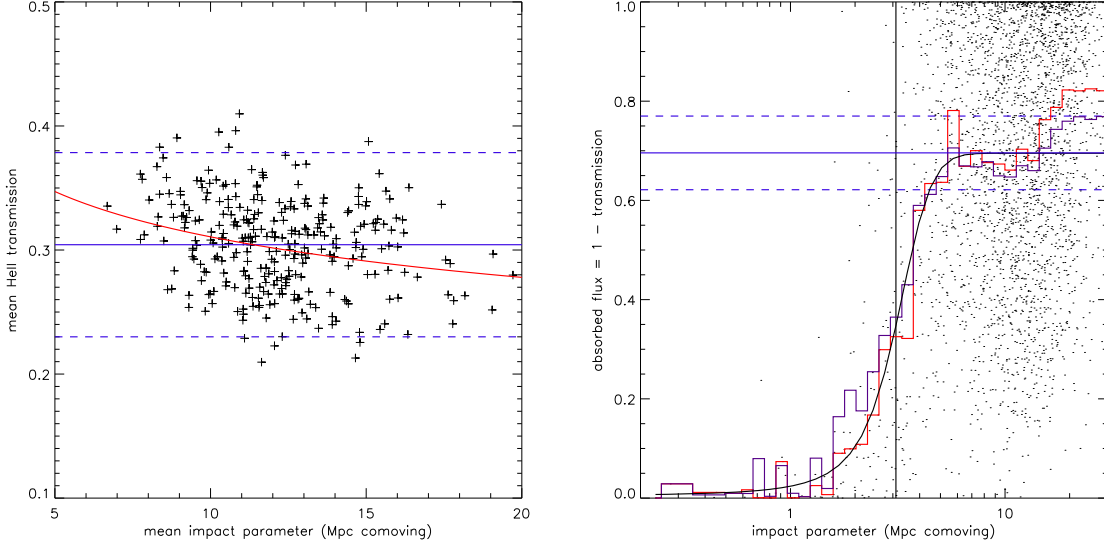


Fig. 9.— On the left panel, we show the scatter plot between the average impact parameter for each sightline in respect to the distribution of the ionizing point sources versus the sightline-specific mean flux. The red line is power law fit to the data with a slope of $s = -0.16 \pm 0.04$. The blue solid (dashed) line shows the average (2σ) He II Ly α transmission from all sightlines at $\bar{z} = 2.5$. The small negative correlation $r = -0.24$ suggests that the mean flux of a sightline is largely insensitive to the average proximity in respect to the distribution of ionizing sources along it’s path. On the right panel, we show the locally absorbed flux (y-axis) at the point of closest proximity to the ionizing source shown on the x-axis. Individual points correspond to the absorbed flux at the pixel of closest distance. The red (blue) histogram is the median (mean) absorbed flux per constant logarithmic bins. Solid and dashed blue horizontal lines are the level of the mean absorption in our sightline sample and the 2σ standard deviation respectively. The solid line is a Fermi-Dirac function that fits the median (red) histogram for impact parameters less that 10 Mpc comoving. The half point of the Fermi-Dirac function is at $d_o = 3.1$ Mpc comoving (shown as a vertical black solid line) and it has a skin width of 0.63 Mpc comoving. Impact parameters along the sightline of $\lesssim 4.5$ Mpc comoving, the point where the absorbed flux falls below the 2σ level of the mean absorption, show a steep sensitivity in the absorbed flux due to the quasar proximity.

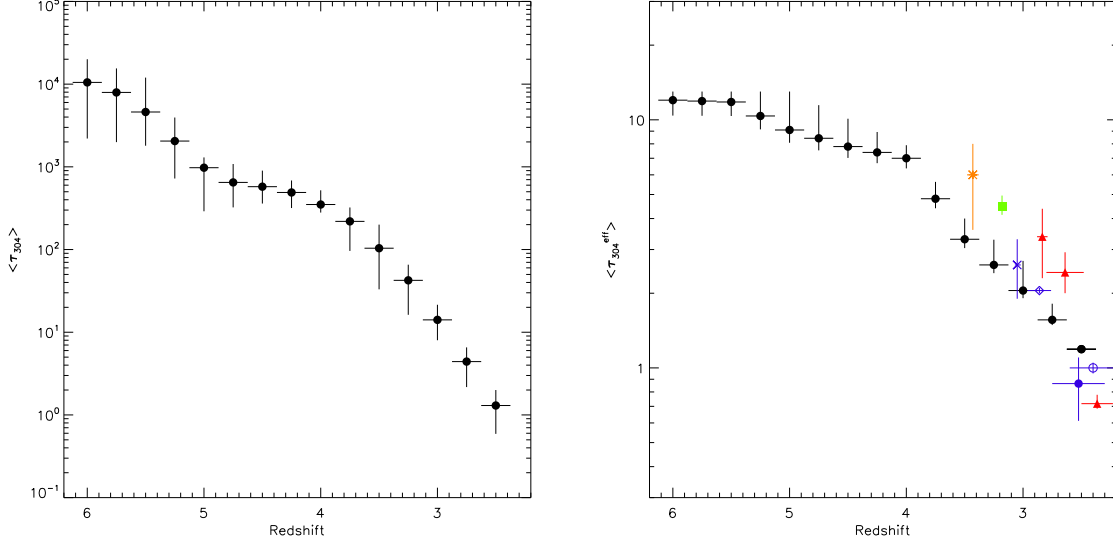


Fig. 10.— We compute the mean optical depth and effective optical depth at selected mean redshift points, from $\bar{z} = 6 - 2.5$ every 0.25 redshift units and in intervals of $\delta z = 0.25$ about the mean redshift. Left Panel: Redshift evolution of the mean pixel Ly α He II optical depth averaged over all lines of sight. The error bars are 1σ standard deviation to the sightline average optical depth. Right Panel: Redshift evolution of the Ly α He II effective optical depth. The error bars in the simulation results are sightline-to-sightline errors estimated from the standard deviation to the average transmission from sightline-specific mean flux. Overplotted are sightline measurements along HE2347-4342 (red triangles), HS1700+6416 (blue circles), HS1157+3143 (blue diamond), PKS1935-692 (blue cross), Q0302-003 (green square) and SDSSJ2346-0016 (orange star). Error bars to these points refer to error estimates of the pixel flux along the sightline specific to the quasar. The HE2347-4342 data from Zheng et al. (2004b) have been resampled to a larger bin size to make it comparable to our data. The redshift profiles of the optical depth point statistics suggest a smooth evolution of the He II reionization epoch.

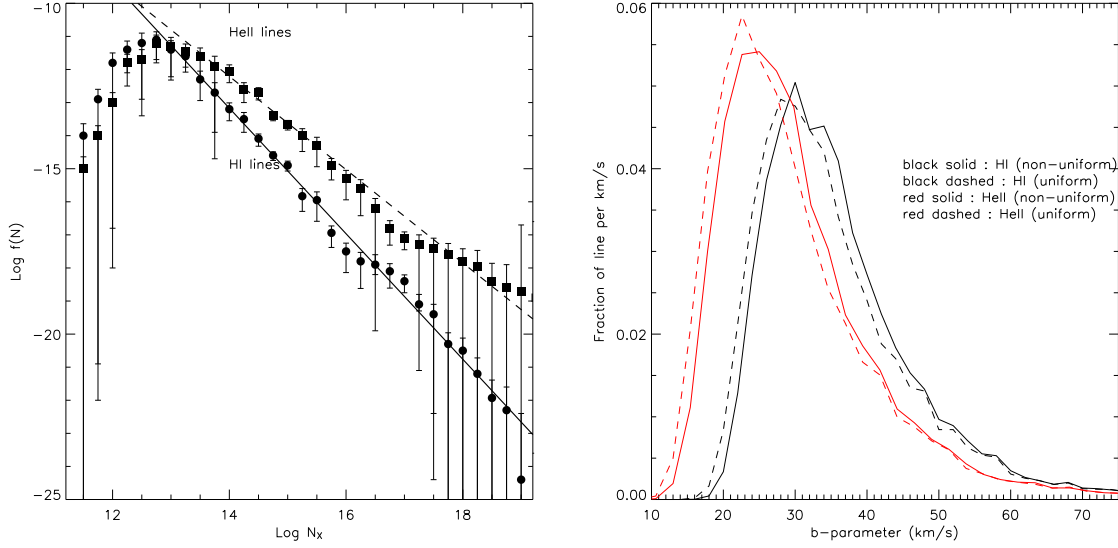


Fig. 11.— Left Panel: Column Density Distributions, $f(N) = \frac{d^2 N}{dz dN_X}$ of H I and He II absorbers between $z = 2.6$ and $z = 2.4$. Circle and square points correspond to the H I and He II column density distribution respectively. Solid (dashed) straight lines (in log-log) show the power law fit to the H I (He II) distribution between column densities $N_X = 10^{13.5} - 10^{15.5} \text{ cm}^{-2}$. The error bars show the 1σ standard deviation to the number of lines per logarithmic column density bin equal to 0.25. Right Panel: Broadening width distributions at $\bar{z} = 2.5$ for He II and H I. The distributions are shown as the fraction of absorption lines per km/s in bins of 2 km/s. Black and red colors correspond to H I and He II distributions respectively. The dashed lines show a reference self-consistent calculation in the optical thin limit using an ionizing uniform UVB. The peaks of non-uniform calculations are offset by $\simeq 1.25$ km/s to the right of the uniform results.

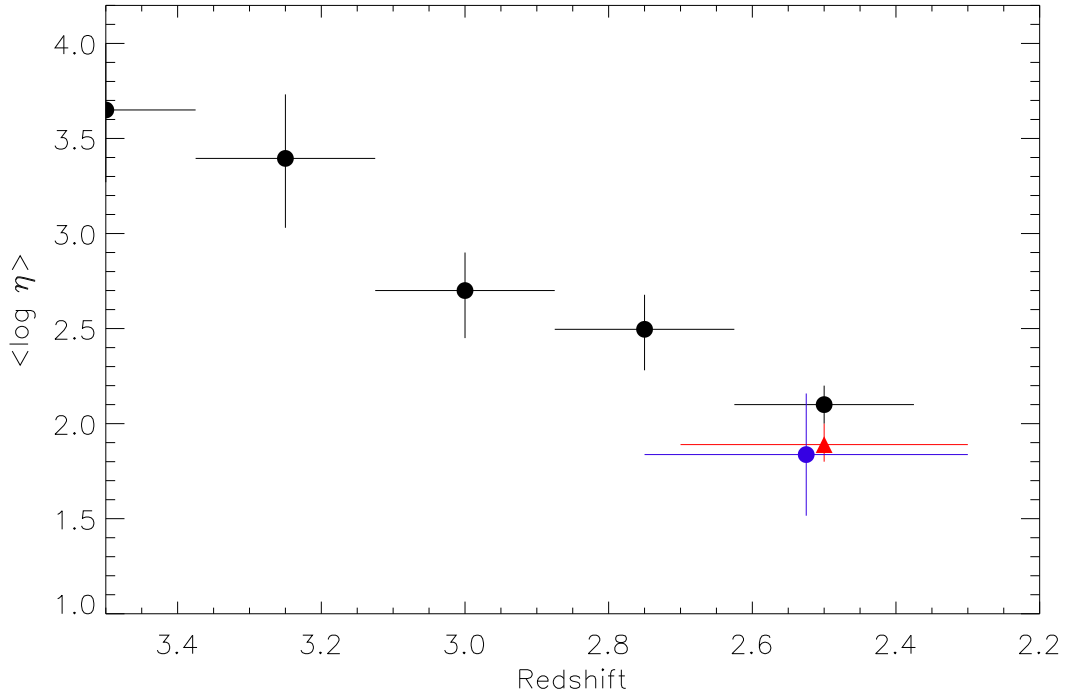


Fig. 12.— Redshift evolution of the η parameter in this simulation. Results are shown as $\langle \log \eta \rangle$ per redshift interval and are obtained as the line column density ratio of He II over H I at low z ($z < 3$) and estimated from the ratio of optical depths at higher redshifts. The filled triangle shows the average estimate between $z = 2.3 - 2.7$ towards HE2343-4342 from Kriss et al. (2001). We also show the data from Fechner et al. (2006) (blue towards HS1700+6416 collapsed into a single redshift interval from $z=2.3-2.75$). Our calculation yields systematically larger values, a result due to the larger estimate of the effective optical depth by $\bar{z} = 2.5$.

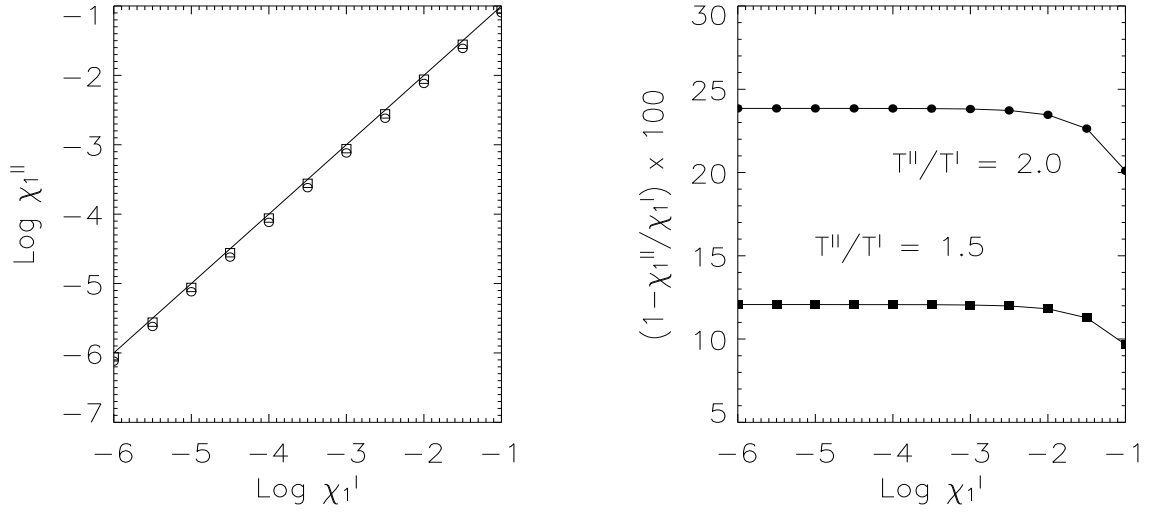


Fig. 13.— Left Panel: $\text{Log } \chi_1^I$ (input) vs. $\text{Log } \chi_1^{II}$ (output) for $T^{II}/T^I = 1.5$ (squares) and $T^{II}/T^I = 2.0$ (circles). Right Panel: Percentage change in the hydrogen neutral fraction vs. $\text{Log } \chi_1^I$.

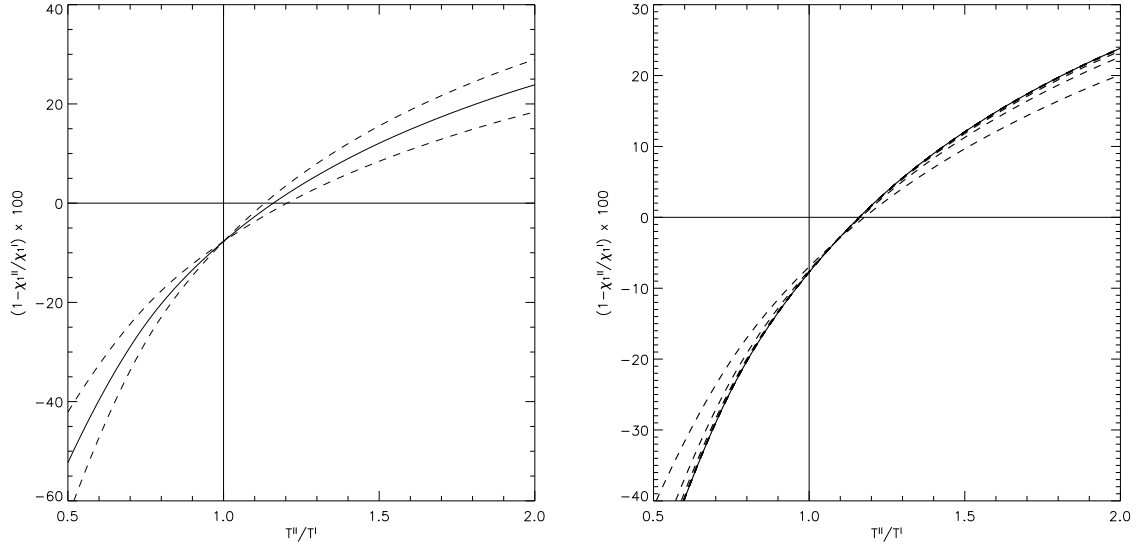


Fig. 14.— Left Panel: Percentage change vs. T^{II}/T^I for three values of the exponent in $\alpha_R^{(1)} \propto T^{-\beta}$. Solid line: $\beta = 0.5$. Upper dashed line at $T^{II}/T^I \geq 1$: $\beta = 0.6$. Lower dashed line at $T^{II}/T^I \geq 1$: $\beta = 0.4$. Right Panel: Percentage change vs. T^{II}/T^I for $10^{-6} \leq \chi_1^I \leq 10^{-1}$. Curves on the upper quadrant from upper to lower (dashed lines) represent an increase in the hydrogen neutral fraction.